A new α-CBC polymer with elevated heat-resistance prepared via catalytic hydrogenation of α-methylstyrene-butadiene-styrene terpolymer over Ni x Pd/NCNT@MFN monolithic catalyst

Chun-Yan Cao
Shao-Kang Qian
Gui-Ping Cao
gpcao@ecust.edu.cn

Jun-Yang Yan
Peng Gao
Shuang Ji

Research Article

Keywords: bimetallic catalyst, α-methylstyrene-butadiene-styrene terpolymer, full hydrogenation, thermal properties

Posted Date: March 5th, 2024

DOI: https://doi.org/10.21203/rs.3.rs-3955112/v1

A new α-CBC polymer with elevated heat-resistance prepared via catalytic hydrogenation of α-methylstyrene-butadiene-styrene terpolymer over Ni_xPd/NCNT@MFN monolithic catalyst

Chun-Yan Cao[a, 1], Shao-Kang Qian[a, 1], Gui-Ping Cao[a, *], Jun-Yang Yan[a], Peng Gao[a], Shuang Ji[a]

[a] UNILAB, State Key Laboratory of Chemical Engineering, East China University of Science and Technology, 130 Meilong Road, Shanghai, 200237, China

[1] First co-authors: Chun-Yan Cao and Shao-Kang Qian

* Corresponding author. E-mail addresses: gpcao@ecust.edu.cn (Gui-Ping Cao)

ABSTRACT

Elevating the heat resistance of the highly transparent cyclic block copolymer (CBC) is of great significance for the synthesis of high-performance polymers. In this study, a novel bimetallic Ni_xPd/NCNT@MFN catalyst was prepared and applied in the hydrogenation of α-methylstyrene-butadiene-styrene (α-SBS) ternary block copolymer. Ni_2Pd/NCNT@MFN exhibited excellent catalytic performance, and after 8 hours of reaction, a new fully hydrogenated polymer, α-CBC, was obtained. The hydrogenation of the butadiene segment in α-SBS became more difficult as the length of the segment increased. The presence of α-methyl resulted in the highest adsorption-activation energy for the α-methylstyrene monomer unit, leading to a longer hydrogenation time with increasing length of this segment. Furthermore, the introduction of α-methylstyrene not only increased the glass transition temperature of the styrene and α-methylstyrene (S) segments in α-SBS, but also increased the glass transition temperature of α-CBC even more after hydrogenation. This conclusion provides valuable theoretical guidance for the synthesis of high-heat-resistant α-CBC polymers.

Keywords: bimetallic catalyst, α-methylstyrene-butadiene-styrene terpolymer, full hydrogenation, thermal properties

1. INTRODUCTION

Styrene-butadiene-styrene triblock copolymer (SBS) is a type of thermoplastic elastomer consisting of styrene (S) and butadiene (B) segments. The fully hydrogenated product of SBS, cyclic block copolymer (CBC),[1,2] has been found to possess high transparency, excellent UV penetrability, and impressive heat resistance.[3] Moreover, it is of great importance to further enhance the thermal property of CBC resin while preserving its high clarity. Selective hydrogenation of B segments in SBS will result in forming a crystalline region of polyethylene (PE) segments, which is beneficial for enhancing the antioxidant properties and heat resistance of polymers.[4] Fully hydrogenated S segments in SBS producing polycyclohexylidene ethylene (PCHE) segments will further increase the glass transition temperature (T_g) due to forming larger cyclohexyl groups.[5] Li et al.[2] investigated the full hydrogenation of SBS and SIS (styrene-isoprene-styrene copolymer), and the resulting products exhibited higher tensile strength, showing that the saturation of the entire polymer segments can improve its mechanical properties. Hahn et al.[6] employed diimine homogeneous catalysts obtained through the pyrolysis of p-toluenesulfonylhydrazine (TSH) modified by tri-n-propylamine (TPA) for the selective hydrogenation of SBS and SIS copolymers. After a reaction of 4 hours, the hydrogenation of the SBS double bond reached 96 %, while the hydrogenation of the SIS double bond was only 64 %. This result indicates that the electron-donating group ($-CH_3$) and the conjugation effect formed by the C=C double bond stabilize the double bond, making it less favorable for hydrogenation. In order to overcome the aforementioned setback, a high-activity catalyst should be considered.

Currently, homogeneous catalysts such as diimine catalysts,[7-9] Ziegler-Natta catalysts,[10] and Wilkinson noble metals,[11] have exhibit high activity in the hydrogenation of B segments of SBS. However, the introduction of sulfur-containing groups by the TSH has been found to impact the purity of the hydrogenation product.[12] Additionally, most homogenous catalysts are expensive, difficult to separate, and have almost no hydrogenation activity toward the benzene ring. Heterogeneous catalysts loaded with noble metals, such as Pd, have excellent hydrogenation activation in the benzene ring. Chang et al.[13] used Pd/Al_2O_3 heterogeneous catalysts to hydrogenate SBS at 180 °C for 25 hours, achieving a benzene ring hydrogenation degree of 76 %. The activation energies of styrene, 1,4-trans, and 1,2-butadiene segments in SBS were 28.9 kJ/mol, 15.2 kJ/mol, and 14.7 kJ/mol, respectively, while calculated, showing that the activation of the benzene ring is more challenging than that of the double bond.

However, the separation of conventional small-particle heterogeneous catalysts remains problematic, and the hydrogenation process suffers from severe viscosity and stickiness effects, leading to limited mass transfer and decreased catalyst activity.[14,15] Consequently, there is an urgent need to identify an efficient hydrogenation catalyst that exhibits high activity, stability, ease of separation, and does not generate any by-products for the application of SBS total hydrogenation. Monolithic catalysts[16] have been extensively studied for their potential use in catalytic hydrogenation applications, specifically in the reduction of unsaturated groups such as C=C double bonds and benzene rings. These catalysts are typically prepared by loading metal particles, such as Ni and Pd, onto the surface of carbon nanotubes, which possess desirable mechanical properties, a large specific surface area, and high stability.[17,18] Luo et al.[19] used the CVD method to in-situ modify carbon nanotube layers on a nickel foam substrate, followed by impregnation of Pd metal, resulting in a Pd/CNTs@NF catalyst. This catalyst was applied to the hydrogenation of nitrile rubber, achieving a hydrogenation degree of 85 % after 6 hours of reaction. Similarly, Feng et al.[20] prepared Pd/CNT@NF using the same method and employed it for the hydrogenation of polystyrene (PS). After 10 hours of reaction, the hydrogenation degree reached 87 %, these results demonstrate the excellent activity of the prepared catalyst. Compared to monometallic catalysts, the introduction of a second transition metal (such as Ni[21-23], Pt[24], Au[25,26] etc.) to create a bimetallic or multimetallic catalyst with Pd not only reduces the consumption of precious metals but also enhances the activity, selectivity, and stability of the nanoparticles through synergistic effects between the metals.[27] In order to further enhance the T_g of the polymer, the α-methyl group is introduced onto the styrene monomer in SBS segment, resulting in a ternary block copolymer of styrene, butadiene, and α-methylstyrene (α-MS) called α-SBS, where styrene and α-methylstyrene form the S segment in a random manner. Hydrogenation of α-SBS will yield α-CBC, which is expected to further improve the thermal properties of the polymer.

However, the application of monolithic bimetallic catalysts for the hydrogenation of the double bond and benzene ring in α-SBS has not been previously reported in the literature, especially since the effect and mechanism of α-methyl on the hydrogenation activity of the benzene ring in the α-methylstyrene monomer unit are unclear. Furthermore, the relationship between the structure and performance of α-SBS before and after hydrogenation is still unclear. In this paper, nitrogen-doped carbon nanotubes were used as carriers, and Ni, Pd bimetals were used as active components to prepare a

monolithic catalyst. The catalytic performance of the catalyst for the hydrogenation of both the double bond and benzene ring in α-SBS was investigated, and the influence of polymer structure on hydrogenation efficiency and the relationship between the structure and thermal properties of the resulting novel polymer, α-CBC, after hydrogenation were explored. These findings will offer valuable insights for the design of efficient hydrogenation catalysts for polymers and inspire the development of new materials.

2. EXPERIMENTAL SECTION

2.1 Materials

$Ni(NO_3)_2{\cdot}6H_2O$ (~98.5 %) was purchased from Shanghai Titan Technology Co., Ltd. $Pd(NO_3)_2{\cdot}2H_2O$ (Pd content: 39.5 wt%) was purchased from Tianjin Kermel Chemical Co., Ltd. Decalin (DHN) was purchased from Jiangsu Anhuai Chemical Technology Co., Ltd. Nickel foam (~75 PPI, 99 % purity) was purchased from Hebei Yichang Wiremesh Materials Co., Ltd. Acetonitrile was purchased from Shanghai Titan Technology Co., Ltd. PB, SBS, and α-SBS were presented by China Petrochemical Co., Ltd. N_2 (99.99 %), O_2 (99.99 %), and H_2 (99.999 %) were purchased from Shanghai Siyuan Gas Industries Co., Ltd. All chemicals with analytical-grade purity were purchased and used directly without further treatment unless otherwise noted. All solutions were prepared with deionized water.

2.2 Preparation and Characterization of Catalysts

The schematic diagram of preparing Ni_xPd/NCNT@MNF catalysts are shown in Fig. 1.

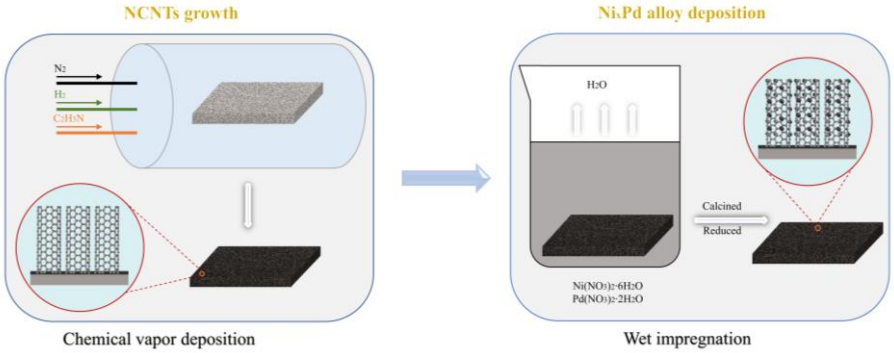

Fig. 1 Schematic preparation of Ni_xPd/NCNT@MFN catalysts

2.2.1 Preparation of NCNT@MFN

The nickel foam (MFN) with a size of 3.5 cm × 2.5 cm × 5 mm was ultrasonicated

in anhydrous ethanol for 30 minutes, washed with distilled water, and dried at 100 °C for 12 hours. NCNTs were in-situ grown on the surface of MFN using the CVD method to synthesize NCNT@MFN. In a typical process, the MFN was treated at 650 °C under N_2 and O_2 in a tubular reactor for 2 hours, after which a mixture of N_2 and H_2 was introduced to reduce the oxide layer of the surface. After 3 hours of reduction, the temperature was lowered to 600 °C under N_2 protection. Nitrogen was passed through acetonitrile liquid to introduce acetonitrile vapor into the tube furnace. NCNTs were grown on the MFN for 2.5 hours using the bubbling method. The oven was cooled to room temperature under N_2 atmosphere to obtain MFN with grown NCNTs, denoted as NCNT@MFN.

2.2.2 Synthesis of Ni_xPd/NCNT@MFN

An equal volume impregnation method was employed to load Ni and Pd nanoparticles onto the surface of NCNT grown on foamed Ni (NCNT@MFN). In a typical procedure to synthesize Ni_xPd/NCNT@MFN, the water absorption capacity of each NCNT@MFN was determined (4.2 g - 4.3 g). Amounts of respective 0.231 g $Ni(NO_3)_2{\cdot}6H_2O$ (Ni precursor) and 0.105 g of $Pd(NO_3)_2{\cdot}2H_2O$ (Pd precursor) were dissolved in deionized water to the actual absorption capacity of each NCNT@MFN mentioned above. The NCNT@MFN absorbed the solution completely, leaving no residue, and the impregnated NCNT@MFN was dried in an oven at 100 °C for 12 hours. The dried NCNT@MFN was placed into a tube furnace, heated to 385 °C under a nitrogen flow, and calcined for 5 hours. The temperature was subsequently lowered to 300 °C, and reduction was carried out under a mixture of N_2 and H_2 for 8 hours simultaneously. After reduction, the catalyst was cooled to room temperature under an N_2 atmosphere to obtain Ni_xPd/NCNT@MFN catalysts, where *x* represents the molar ratio of nickel to palladium.

2.2.3 Characterization of Carriers and Catalysts

Morphologies and microstructures of MFN and NCNT@MFN were observed using S-3400 N scanning electron microscopy (SEM), and the elemental components on the surface of NCNT@MFN were analyzed qualitatively and semi-quantitatively using energy dispersive X-ray spectrometry (EDS). High-resolution transmission electron microscopy (TEM) JEM-2100 was performed to observe the morphology and particle size distribution of the metallic Ni_xPd nanoparticles over the carbon support at an accelerating voltage of 200 kV. TEM species were prepared by depositing droplets of suspension on a standard copper grid after ultrasonic treatment of samples in ethanol. The surface composition and chemical speciation of the samples were further analyzed using an ESCALAB 250Xi X-ray photoelectron spectrometer (XPS) with an excitation source of Al Ka rays. Crystalline structures and compositions of the carrier and catalyst

were studied using a D/max2550VB/PC X-ray diffractometer (XRD, RIGAKU) with an X-ray source of CuKα (40 kV, 30 mA), a scanning rate of 10 °/min, a scanning step of 0.02°, and a scanning range from 5° to 80°.

2.3 Catalytic Hydrogenation of α-SBS

The hydrogenation reaction was carried out in a 500 mL high pressure reactor, as shown in Fig. 2.

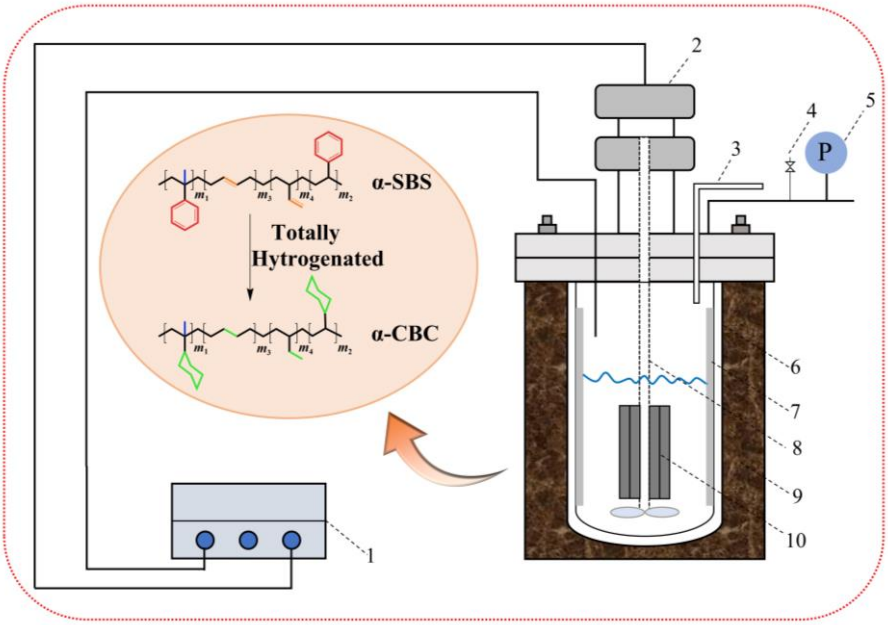

Fig. 2 Schematic diagram of α-SBS hydrogenation in high pressure reactor (1. temperature and speed controller; 2. stirring motor; 3. H_2 and N_2 air inlet; 4. pressure reducing valve; 5. pressure gauge; 6. high pressure reactor; 7. baffle plate; 8. stirring shaft; 9. heating jacket; 10. catalysts)

A total of 150 g of a 3 wt% α-SBS DHN solution was introduced into the reactor. The reaction was conducted at 180 °C and 6 MPa hydrogen pressure, using four pieces of Ni$_x$Pd/NCNT@MFN catalysts as stirring paddles with a stirring speed of 500 rpm. After the reaction, the hydrogenated product was precipitated three times in ethanol and dried. The hydrogenation degree of the C=C double bond (HD_B) was analyzed by iodometric titration, as calculated using the Equation (1).

$$HD_B = \frac{c_{B0} - c_B}{c_{B0}} \times 100\% \quad (1)$$

Where c_{B0} (mol/L) was the concentration of C=C double bond at initial time and c_B (mol/L) was the concentration of C=C double bond at a certain time.

The hydrogenation degree of the benzene ring (HD_S) was analyzed by a UV-visible spectrophotometer at a wavelength of 261.5 nm (the methyl group had no effect on the UV absorption wavelength of the benzene ring), which can be calculated by Equation

(2).

$$HD_S = 1 - \frac{c_S}{c_{S0}} \times 100\% \quad (2)$$

Where c_{S0} (mol/L) was the concentration of benzene ring at initial time and c_S (mol/L) was the concentration of benzene ring at a certain time.

2.4 Polymer Characterization

A NETZSCH 200F3 differential scanning calorimeter (DSC) was used to monitor the thermal behavior of all the samples before and after hydrogenation at a heating or cooling rate of 10 °C/min, unless otherwise noted. The samples were first heated to 300 °C under an N_2 atmosphere and held for 3 minutes to eliminate thermal history. Subsequently, the samples were cooled to −150 °C and heated again to 300 °C to obtain the second run melting curve, which was used for determining the melting temperature (T_m), melting enthalpy (ΔH_m), and glass transition temperature (T_g). The crystallinity can be calculated by Equation (3).

$$\chi_c = \left(\frac{\Delta H_m}{\Delta H_m^0} \right) \times 100\% \quad (3)$$

Where ΔH_m^0 is the fusion enthalpy of the PE with 100 % crystallinity, which is 0.293 J/kg.[28,29]

BRUKER PLUS 600M NMR spectroscopy (^{1}H NMR and ^{13}C NMR) was used to analyze the compositional and structural differences between the reactants and hydrogenation products using TMS as the internal standard. Chemical shifts for ^{1}H and ^{13}C NMR were referenced to residual signals from $CDCl_3$ (^{1}H: δ = 7.26 ppm and ^{13}C: δ = 77.23 ppm). A minimum of 150 scans were collected for each spectrum.

FTIR spectra were recorded on a Nexus 470 Fourier transform infrared spectrometer in ATR test mode to analyze the structural differences in functional groups between the reactants and hydrogenated products. The specific testing method for infrared spectroscopy involved taking 10 mg of the sample and 1 g of dried KBr powder in a mortar, grinding them together, pressing the prepared sample using a tablet press, dehydrating the sample in a vacuum environment at 300 °C for 4 hours, and collecting the infrared transmission spectrum of the sample. The wave number range was set from 3500 cm^{-1} to 500 cm^{-1}, with a resolution of 2 cm^{-1} and 32 scans.

2.5 Simulation Calculation

In order to investigate the interaction between bimetallic catalysts and the α-SBS, and the activation differences of different monomer units on the catalyst surface, the adsorption of benzene rings and double bonds in α-SBS on the active metal surface was simulated using the density functional theory (DFT) framework in the CP2K program package. It should be noted that four representative monomer units in the α-SBS

segment were selected: α-methylstyrene (m_1), styrene (m_2), 2,3-butadiene (m_3), and 3,4-butadiene (m_4), and it is assumed that they are adsorbed on the catalyst surface in a hydrogen-saturated form. The Perdew, Burke, and Ernzerhof (PBE)[30] exchange-correlation functional was used to solve the Kohn-Sham equations within the generalized gradient approximation (GGA), and the DFT-D3[31,32] (Grimme) empirical correction was used for long-range London dispersion (van der Waals attraction). All elements were described using the Goedecker-Teter-Hutter pseudopotential and double- ζ MOLOPT basis sets (DZVP-MOLOPT-SR-GTH). The electronic energy optimization accuracy was set to 10^{-6} eV, the force accuracy on each atom was less than 0.03 eV/Å, and the energy cutoff was set to 450 eV. In this section, a periodic PdNi metal model was constructed, and four monomer unit models were built on its surface to study the adsorption process on the metal surface. The model size was 13.01 Å × 11.27 Å × 30.00 Å, and the first Brillouin zone was sampled using a (3 × 3 × 1) Monkhorst-Pack k-point grid.

3. RESULTS AND DISCUSSION

3.1 Structure Composition of Ni_xPd/NCNT@MFN

The microscopic morphologies of MFN and NCNT@MFN are observed using SEM which are shown in Fig. 3. It can be seen from Fig. 3(a) that the surface of the original MFN is smooth. But after growing nitrogen-doped carbon nanotubes, the surface of MFN exhibits roughness and is covered with a uniform carbon layer (Fig. 3(b) and (c)). Moreover, the nickel foam skeleton remains intact without any signs of fracture. As illustrated in Fig. 3(d) - (f), the carbon nanotubes display a clear tubular structure with an average outer diameter of 23.1 nm and a standard deviation of 0.38 nm (Fig. 3(e)), which indicates that the size distribution of the grown NCNTs is very uniform in our CVD process.

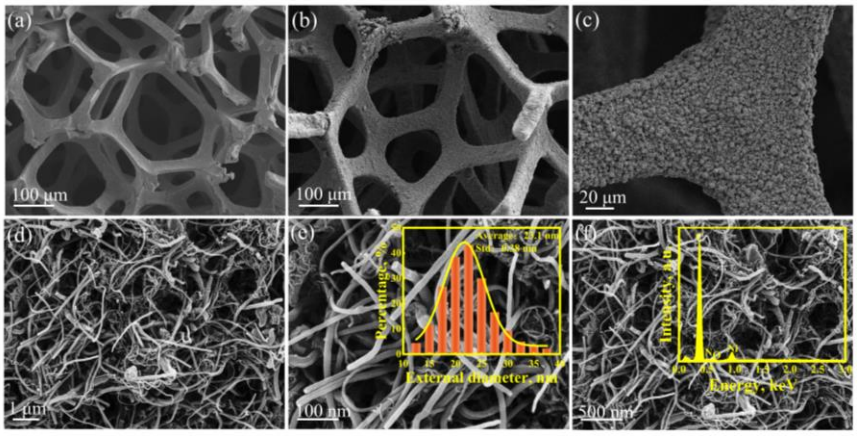

Fig. 3 SEM images of samples: (a) Skeleton of original nickel foam; (b) (c) Skeleton of NCNT@MFN; (d) NCNTs formed on nickel foam surface; (e) Statistical distribution of NCNTs outer diameter; (f) Elemental distributions of EDS

The elemental composition of NCNT@MFN is characterized by EDS analysis, as shown in Fig. 3(f), which indicates that the samples are primarily composed of four elements: C, N, O, and Ni. Among these elements, C has the highest elemental characteristic peak. Furthermore, the presence of the characteristic peak of N confirms the successful doping of carbon nanotubes with elemental nitrogen. On the other hand, the elemental oxygen originated from a small quantity of nickel oxide in NCNT@MFN. Due to the limited amount of carbon nanotubes growing in apical mode,[33] some of the nickel nanoparticles were lifted up, leading to the distinct peak of elemental Ni in EDS. However, it was noteworthy that NCNT@MFN did not exhibit any shedding of NCNTs after ultrasonication, suggesting that the NCNTs were firmly anchored to the surface of the MFN skeleton primarily through root growth. Table 1 presents the mass percent and atomic percent of elements C, N, O, and Ni in the NCNT@MFN sample. The N/C mass ratio is found to be 2.17 wt%, while the N/C atomic ratio is 2.34 at%.

Table 1 Elemental content of C, N, O, and Ni in NCNT@MFN sample

Element	Weight ratio, wt%	Atomic ratio, at%
C	95.23	96.14
N	2.07	2.25
O	0.52	0.50
Ni	2.18	1.11

TEM is employed to investigate the structure and the dispersion of Ni_xPd nanoparticles, as shown in Fig. 4(a) and (b). Fig. 4(a) presents that the Ni_xPd nanoparticles exhibit a uniform distribution anchored on the outer surface of the nitrogen-doped carbon nanotubes, assuming a spherical shape, with an average particle size of 3.91 nm and a standard deviation of 0.07 nm. In Fig. 4(b), the crystal face of the Ni_xPd particles clearly displays a measured spacing of 0.216 nm, which falls between the crystal spacing of Pd(111) (0.225 nm) and Ni(111) (0.204 nm),[25] notably indicating the formation of Ni_xPd alloys rather than separate Ni particles or Pd particles.

The crystal structures of four samples, MFN, NCNT@MFN, Pd/NCNT@MFN, and Ni_xPd/NCNT@MFN, are analyzed using XRD, as shown in Fig. 4(c) and (d). In Fig. 4(c), the corresponding diffraction peaks at 2θ of 44.5°, 51.8°, and 76.4° are identified as Ni(111), Ni(200), and Ni(220) (PDF#04-0850) crystal surfaces, respectively. Following the growth of NCNTs, the diffraction peak of the C(002) crystal face appears at 26.4°, indicating that the MFN surface underwent modification with NCNTs, which is consistent with the SEM results. Fig. 4(d) reveals the presence of Pd(111) and Pd(200) (PDF#46-1043) crystal surfaces at 40.1° and 46.6° in the Pd/NCNT@MFN sample, respectively.[34] In the Ni_xPd/NCNT@MFN sample, the diffraction peaks of Pd are observed at 40.5° and 46.9°. A comparison of the two

samples indicates a slight forward shift of 0.3° - 0.4° in the diffraction peaks corresponding to Pd in the Ni_xPd catalyst, while no change is observed in the carrier. This shift can be attributed to the doping of Ni atoms, which have a smaller atomic radius (0.124 nm), into the Pd lattice (0.139 nm).[24,35] Therefore, the Ni_xPd alloy reveals a smaller lattice constant than Pd/NCNT@MFN, leading to a reduction in lattice spacing and causing the observed shifts in the Pd diffraction peaks. The formation of alloys is verified through the employment of both XRD and TEM analyses.

To further analyze the chemical and surface electronic properties of Ni_xPd/NCNT@MFN, the XPS spectra are shown in Fig. 4(e) - (h). The XPS full spectrum in Fig. 4(e) conforms to the presence of C 1s, Pd 3d, O 1s, and Ni 2p. Integration of the Ni and Pd peaks results in a Ni/Pd atomic number ratio of 2.06, which corresponds to the molar ratio of Ni and Pd atoms used in the catalyst preparation process. Fig. 4(f) - (h) displays the core-level XP spectrum of C 1s, Ni 2p, and Pd 3d. The splitting of the C 1s peak reveals three distinct peaks at the binding energy (BE) of 284.8 eV (C=C), 260.1 eV (C−O), and 289.5 eV (C−N). In Fig. 4(g), two prominent peaks at the BE of 856.1 eV and 873.3 eV are observed, which correspond to Ni 2p3/2 and Ni 2p1/2, respectively. Additionally, two more satellite peaks at the BE of 861.3 eV and 880.3 eV are observed, indicating the presence of Ni^{2+} in Ni_xPd/NCNT@MFN.[36] The chemical state of Pd is depicted in Fig. 4(f), which displays four distinct characteristic peaks: Pd^{2+} 3d5/2, Pd^0 3d5/2, Pd^{2+} 3d3/2, and Pd^0 3d3/2. These peaks are observed at the BE of 336.88 eV, 335.48 eV, 342.28 eV, and 340.70 eV, respectively. In comparison to monometallic catalysts,[34] the binding energy of Pd^0 in Ni_xPd/NCNT@MFN is shifted towards positive values. This shift can be attributed to the incorporation of Ni into the Ni_xPd particles, resulting in electron transfer between Pd and Ni during the formation of the metallic bond Ni-Pd.[25] The calculated atomic content of Pd^0 is found to be 87.2 at%, which indicates that a majority of the Pd existed in the 0-valence state. However, the presence of some Pd^{2+} may be attributed to oxidation. According to the Horiuti-Polanyi mechanism,[37] the metallic state Pd^0 is capable of dissociating H_2 into active H·, which serves as the catalytically active center for the hydrogenation reaction.

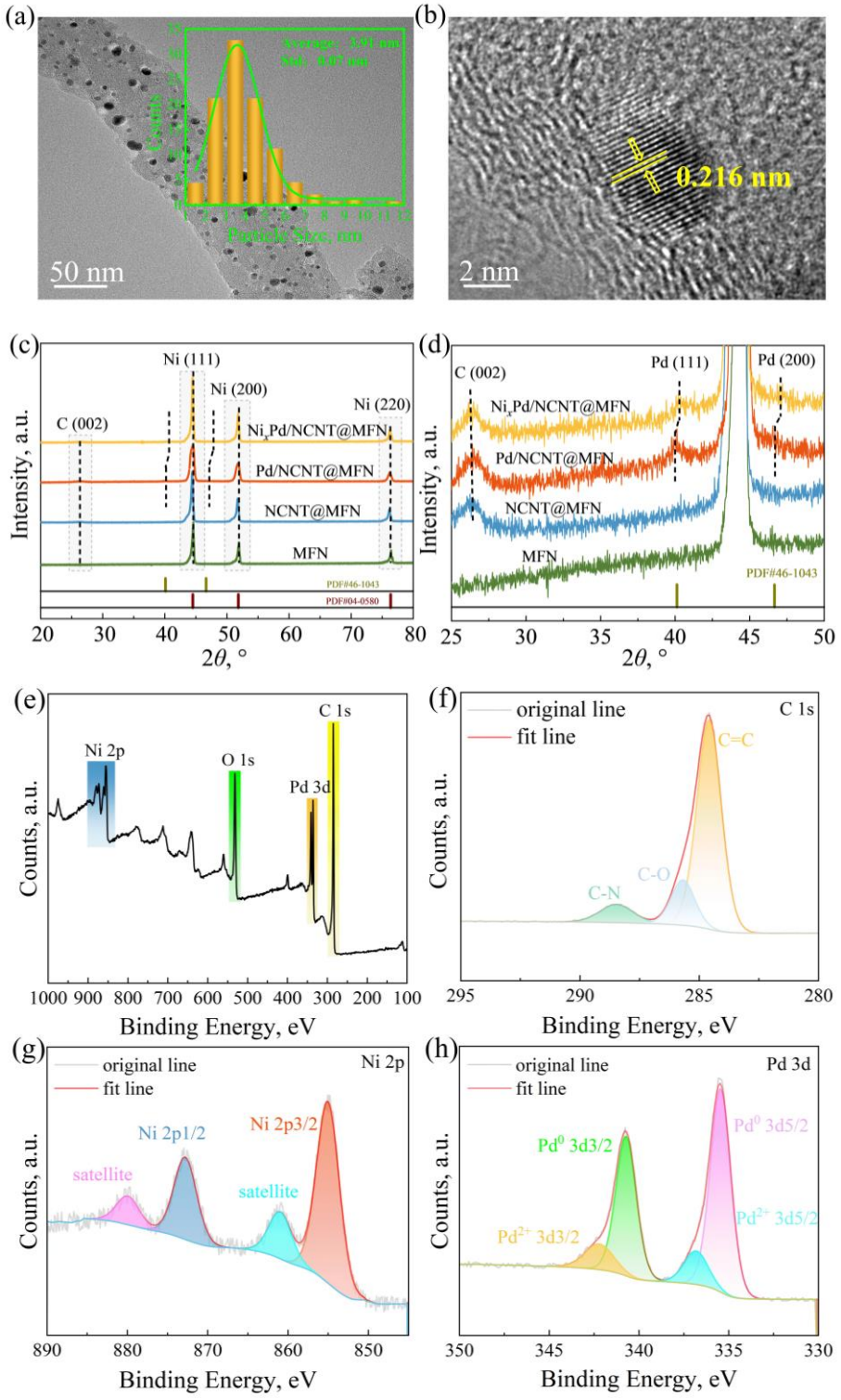

Fig. 4 Structural characterization of Ni_xPd/NCNT@MFN catalysts: (a) TEM images and size distribution of Ni_xPd nanoparticles; (b) The crystal face spacing of Ni_xPd nanoparticles; (c) XRD patterns of carrier and catalyst, (d) is the local enlarged image of (c); (e) Full XPS spectrum of Ni_xPd/NCNT@MFN; (f) (g) (h) XPS peak-fitting profiles of C 1s, Ni 2p, and Pd 3d, respectively

3.2 Catalytic Performance of Ni_xPd/NCNT@MFN

The impact of Ni/Pd atomic ratios on the catalytic activities of the benzene ring

and C=C double bond in SBS is first investigated, as illustrated in Fig. 5. By fixing the Pd loading, the Ni/Pd ratio was varied from 1 to 2, resulting in an increase in HD_S from 63.8 % to 87.1 %. However, further increasing the Ni/Pd ratio to 3 led to a decrease in HD_S to 78.6 %. The HD_B also exhibited a similar trend with the Ni/Pd ratio. The findings of this study indicate that the activity of the catalyst is affected by the ratio of Ni/Pd. Chen et al.[38] examined the effect of the Ni/Pt atomic ratio on the catalytic hydrogenation of the double bond and benzene ring using Ni-Pt@γ-Al_2O_3. The number of Ni-Pt ligands increased with the increase in Ni content, resulting in an increase in hydrogenation activity. Similarly, the formation of Ni-Pd metallic bonds in Ni_xPd/NCNT@MFN is found to be closely associated with the Ni/Pd atomic ratio. Within a certain range, catalytic activity increases as the Ni/Pd atomic ratio increases. However, excessive Ni content can lead to excess Ni atoms covering the alloy surface, hindering the alloy catalyst from contacting the reactants and resulting in a decrease in catalytic activity.

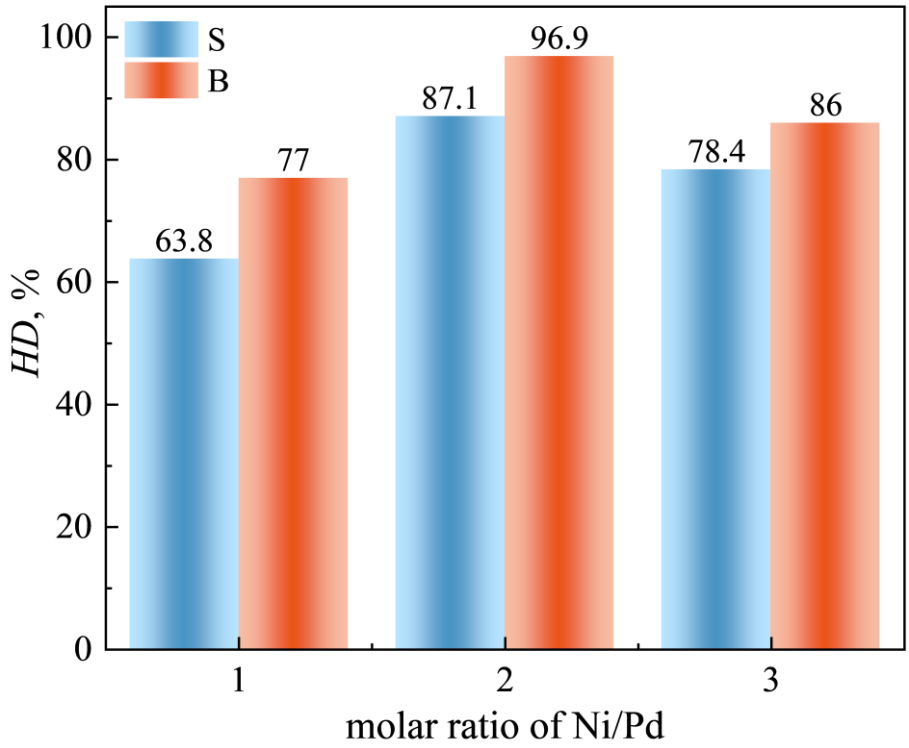

Fig. 5 Effect of the Ni/Pd atomic ratio on catalytic activity in Ni_xPd/NCNT@MFN (reaction conditions: 180 °C reaction temperature, 6 MPa H_2 pressure, 3 wt% SBS concentration, 4 pieces catalysts usage, 7 hours)

When Ni_2Pd/NCNT@MFN is used as a catalyst for the hydrogenation of α-SBS, both the S segment and the B segment are simultaneously hydrogenated. Obviously, the active sites of the catalyst exhibit different hydrogenation activities towards the benzene ring of the S segment and the C=C double bond of the B segment. Therefore, we first

investigated the hydrogenation process of each homopolymer. A series of studies on the hydrogenation of PS using different carriers loaded with Pd monolithic catalysts have been conducted in our group. Han et al.[39] have innovatively prepared open-cell TiO_2 foam ceramic (CF) loaded Pd monolithic catalysts to enhance the internal mass transfer behavior and effectively hydrogenate PS. Subsequently, Feng et al.[40] have prepared Pd/CNTs@CFs, which are carbon nanotube modified Fe-doped CFs loaded with Pd catalysts, and achieved a degree of hydrogenation of 53 % after 10 hours of reaction. Moreover, a Pd@CNT/FN catalyst was prepared by changing the carrier to nickel foam (FN), resulting in 87 % hydrogenation at 180 °C and 5.8 MPa for 10 hours.[20] The use of monolithic Pd catalysts has resolved the issues of scale effect, conformational effect, and separation difficulties during PS hydrogenation. However, these catalysts have not yet been applied to the hydrogenation of α-SBS.

For comparison, the catalytic hydrogenation of the butadiene homopolymer polybutadiene (PB) was carried out using DHN as a solvent. The behaviors of Ni_2Pd/NCNT@MFN, Pd/NCNT@MFN, Ni/NCNT@MFN, NCNT@MFN, and MFN catalysts in the hydrogenation of PB were investigated under the following conditions: temperature of 160 °C, pressure of 6 MPa, PB concentration of 2.5 wt%, and catalyst loading of 4 pieces, as shown in Fig. 6. It is evident that neither the NCNT@MFN nor the MFN can catalyze the hydrogenation of PB in the absence of the active metals Ni or Pd. Furthermore, the Ni/NCNT@MFN catalyst exhibited very low activity, with a hydrogenation degree of only 3.1 % after 4 hours of reaction. Ni_2Pd/NCNT@MFN was notably found to be more active than Pd/NCNT@MFN. Fig. 6(a) displays the reaction rate of these two catalysts over time. At the start of the reaction, Ni_2Pd/NCNT@MFN has a reaction rate 139.3 $\mathrm{mmol}/\left(g_{Pd}\cdot h\right)$ higher than that of Pd/NCNT@MFN. As the reaction proceeds, the reaction rates of both catalysts gradually decrease, and finally, the reaction rate decreased to 17.7 $\mathrm{mmol}/\left(g_{Pd}\cdot h\right)$ at 10 h of reaction. This is clearly due to the synergistic effect[21] of the Ni_2Pd alloy formed in the early stage of the reaction in Ni_2Pd/NCNT@MFN, which enhances the catalytic activity of the metal nanoparticles. As the reaction progresses, the length of the PE segment with crystallinity[41,42] increases, which causes a decrease in the solubility of the polymer, decreasing the residence time of the C=C to be hydrogenated on the catalyst surface. This ultimately results in a significant decrease in the rate of hydrogenation. Therefore, in SBS or α-SBS, a shorter butadiene segment length will favor the hydrogenation of this segment.

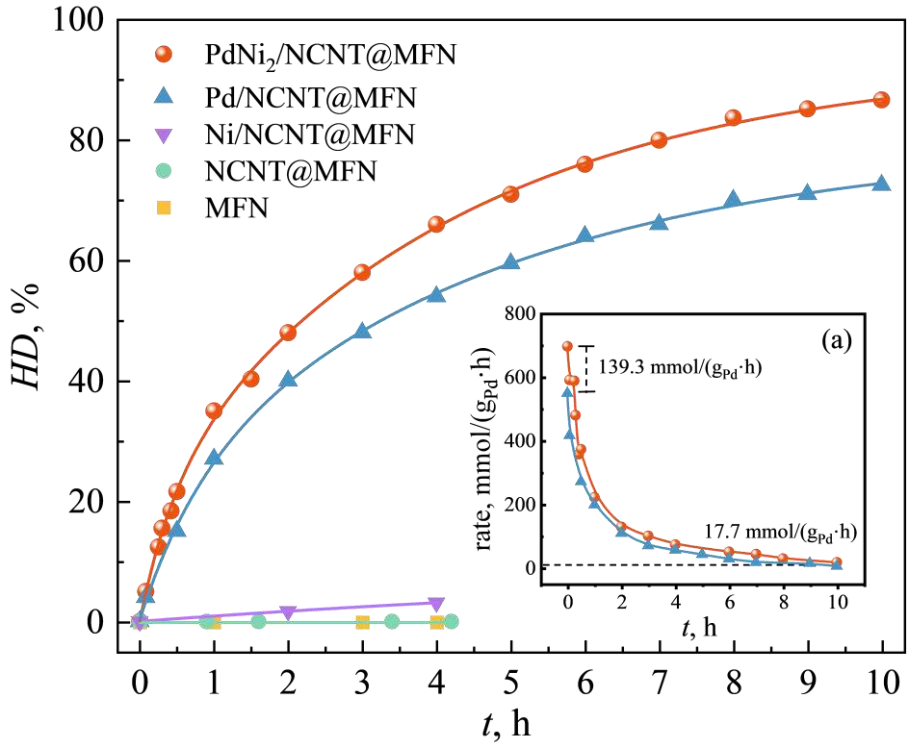

Fig. 6 The relation of PB hydrogenation degree with time; (a) Reaction rate versus time plots

The hydrogenation of SBS and α-SBS by Ni_2Pd/NCNT@MFN was investigated when both S segments and B segments were present in the polymer. Since the content and length of different structures in the polymer have a significant effect on hydrogenation. Therefore, prior to hydrogenation, the content of various structures in PB, SBS, and α-SBS samples was quantitatively analyzed using ^{1}H NMR (Fig. S1). The relative molar content of each component in the polymer and the length of each segment were calculated based on the M_n, as shown in Table 2.

Table 2 Structural composition and chain length in different samples

Polymer	χ, mol%					M_n, $\times10^4$g/mol	$L_{\alpha\text{-MS}}$	L_S	L_B
	α-MS	PS	1,4-trans	1,4-cis	1,2-vinyl				
PB	0	0	0	98.2	1.8	4.5	0	0	803.6
SBS	0	35.0	23.0	29.5	12.5	5	0	168.9	580.4
α-SBS1	1.5	75.9	8.5	11.4	2.7	15	19.1	1094.7	605.4
α-SBS2	1.8	72.2	7.1	16.3	2.6	14	21.4	971.9	650.0
α-SBS3	2.4	69.6	11.6	13.2	3.2	14	28.5	936.9	700.0
α-SBS4	2.6	72.4	6.7	14.9	2.4	12	26.4	835.4	514.3
α-SBS5	3.3	71.7	6.6	15.9	2.5	12	33.6	827.3	535.7
α-SBS6	4.1	71.7	6.2	15.5	2.5	7	24.3	482.6	302.5

χ is the structural composition content in different samples, derived from ^{1}H NMR, where α-MS is α-methylstyrene; 1,4-trans, 1,4-cis, and 1,2-vinyl are the three segments of trans-1,4-butadiene, cis-1,4-butadiene, and 1,2-butadiene respectively; M_n is the number average molecular weight, $\times10^4$ g/mol; $L_{\alpha\text{-MS}}$, L_{PS}, and L_{PB} are the lengths of α-PS, S, and B segments, respectively.

The variation of the benzene ring and double bond hydrogenation degree with time in SBS is shown in Fig. 7. At 6 hours, the HD_S and HD_B were 77.6 % and 87.9 %,

respectively. At 8 hours, the HD_S was 94.5 % and the HD_B was 100 %, indicating that the hydrogenation activity of the C=C double bond was significantly higher than that of the benzene ring. This can be attributed to the greater stability of the large π-bonds in the benzene ring compared to those in the C=C double bond.[13,43] In addition, the large rigidity and size of the benzene ring segment[44] created spatial site resistance, making it more challenging for the structure to bind to the catalyst and undergo hydrogenation under the same conditions. For the S segment in SBS, which has a length of 168.9, full hydrogenation is achieved after 9 hours of reaction. In our previous work using pure PS for hydrogenation, the segment length was 1242, and the hydrogenation degree was only 65 % after 9 hours of reaction using Pd@CNT/FN.[20] Compared with the PB hydrogenation in Fig. 6, the chain length of the high cis-PB is 803.6, while the length of the B segment of SBS containing 80.8 % 1,4-structures is 580.4. Notably, the length of the B segment in SBS is lower than that of pure PB, and the PE segment generated after hydrogenation is shorter. As a result, the full hydrogenation of the C=C double bond in SBS only required 8 hours, whereas pure PB could not achieve 100 % hydrogenation. These results illustrate that the hydrogenation rates of the S and B segment are both influenced by the chain length. The longer chains result in higher solution viscosity, leading to significant viscous and adhesion effects during hydrogenation.[3]

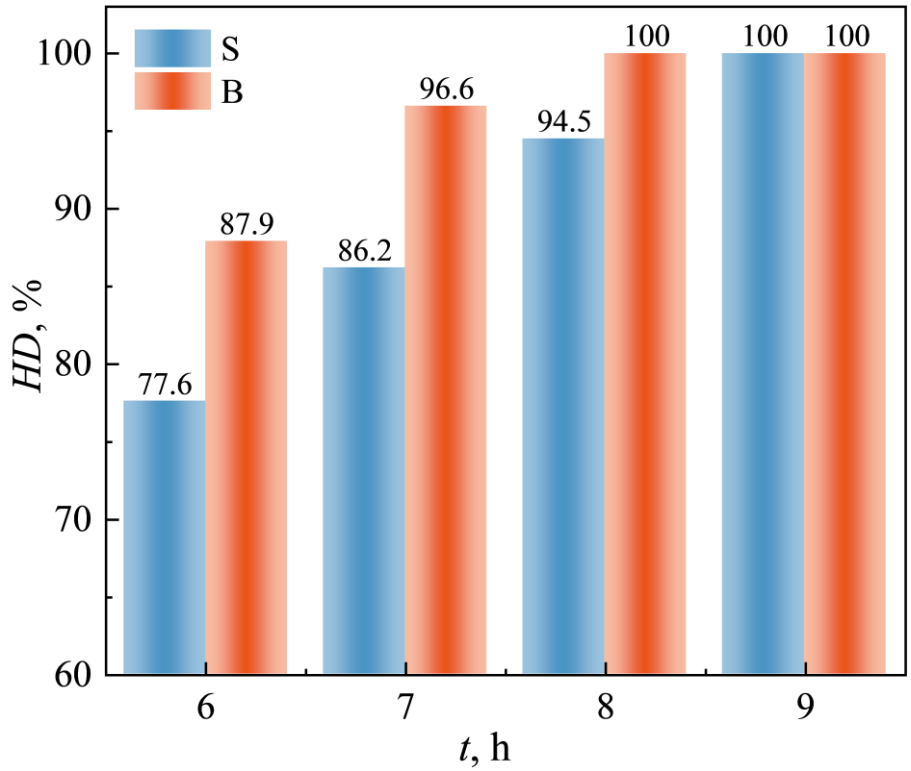

Fig. 7 Change of hydrogenation degree of SBS benzene ring and double bond with time

Fig. 8 shows the results of the hydrogenation degree of the benzene ring and

double bond in α-SBS over time. Comparison of Fig. 8(a) and (b) reveals that it takes 10 hours to achieve 100 % hydrogenation of the benzene ring in α-SBS1, while the double bond requires 9 hours. This indicates that Ni_2Pd/NCNT@MFN exhibits remarkable hydrogenation activity for both the benzene ring and double bond, with the double bond showing higher susceptibility to hydrogenation compared to the benzene ring. Further analysis of the hydrogenation of different α-SBS benzene rings in Fig. 8(a) shows variations in the hydrogenation time of α-SBS1 - 6. For example, α-SBS6 reaches 100 % hydrogenation in only 8 hours, which is clearly related to the length of the S segment in α-SBS.

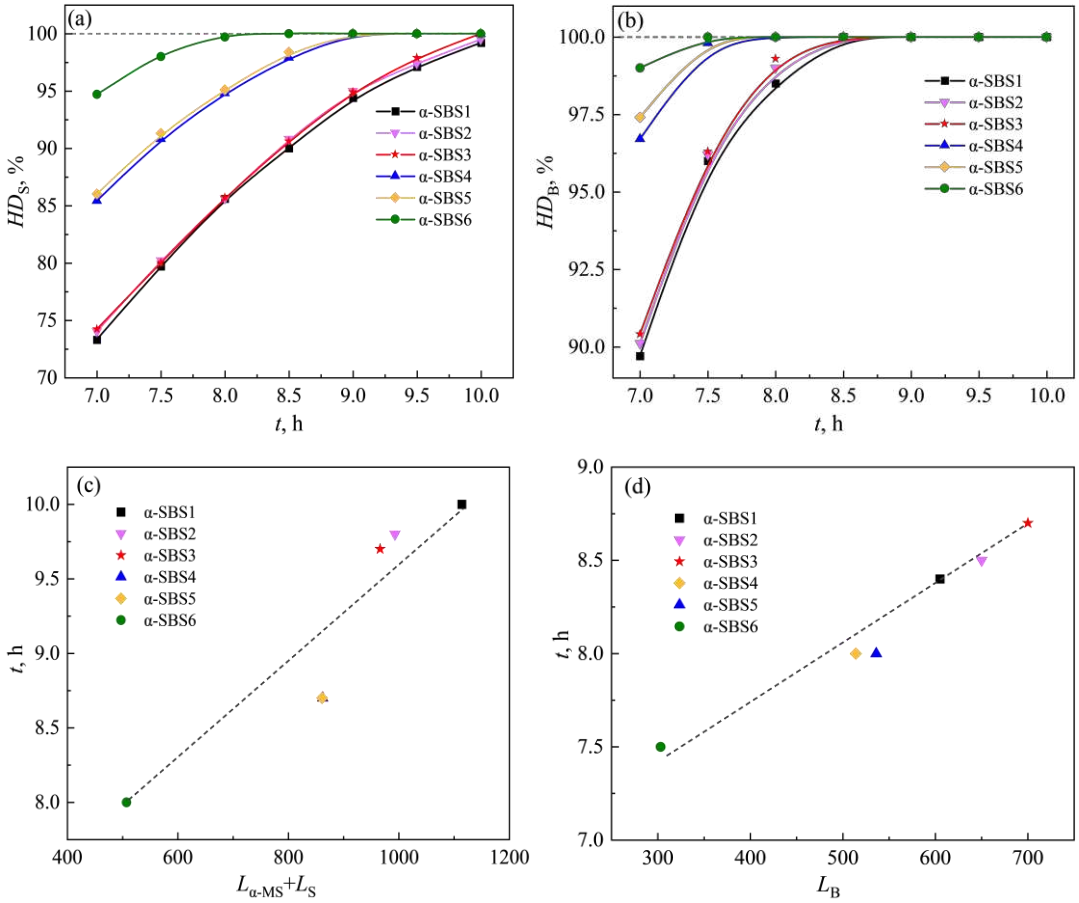

Fig. 8 (a) (b) Degree of hydrogenation of the benzene ring and double bond of the α-SBS sample with time; (c) (d) Time required for 100 % hydrogenation with the length of the segment

To visualize this relationship, the time required for full hydrogenation of α-SBS is plotted against the length of the S segment, as depicted in Fig. 8(c). The plot indicates an approximately clear linear increase in t with respect to ($L_{α-MS}$+L_S). Fig. 8(c) shows that α-SBS6, with α-MS and S segment lengths of 506.9, requires 8 hours to fully hydrogenate, which is 2 hours less than that of α-SBS1 (corresponding to α-MS and S segment lengths of 1113.8). In comparison to the results in Fig. 8(d), during the hydrogenation of the B segment, the hydrogenation activity of the C=C double bond in segments of different lengths remained the same, but the solubility in the solvent varied. Specifically, the longer the L_B, the lower the solubility, resulting in a more curled chain

and increased difficulty in hydrogenation. Additionally, as hydrogenation progressed, the B segment became saturated, forming a PE segment with crystalline properties, which increased the difficulty of hydrogenation. This phenomenon is supported by the difficulty in achieving 100 % hydrogenation in pure PB hydrogenation, as demonstrated in Fig. 6. Similar to the effect of S segment length on the hydrogenation rate, a longer B segment length results in a slower hydrogenation rate.

Additionally, the α-methylstyrene segment and the styrene segment in α-SBS are not isolated but have a mutual influence on hydrogenation. Multiple linear regression is an effective method to judge the strength of the interaction between factors. The following multivariate Equation (4) is established, with $L_{\alpha\text{-MS}}$ and L_S as the independent variables and the time required for full hydrogenation as the dependent variable.

$$y = \beta_0 + \sum_{i=1}^{m} \beta_i x_i + \sum_{i=1}^{m} \beta_{ii} x_i^{\,2} + \sum_{\substack{i=1 \\ j\geq 1}}^{m} \beta_{ij} x_i x_j + \varepsilon_j \tag{4}$$

Where y is the model value of the time required for 100 % hydrogenation. β_0, β_i, β_{ij}, and β_{ii} are the regression coefficient. ε is the random error. x_i is the primary term of the factor. x_i^2 is the quadratic term of the factor. $x_i x_j$ is the interaction term of the factor. Use Equation (5) - Equation (9) to normalize $L_{\alpha\text{-MS}}$ and L_S, so that the intervals of x_1 and x_2 are [−1, 1].

$$x_1 = \frac{L_{\alpha\text{-MS}} - L_{\alpha\text{-MS0}}}{\Delta L_{\alpha\text{-MS0}}}, \quad x_2 = \frac{L_S - L_{S0}}{\Delta L_{S0}} \tag{5}$$

$$L_{\alpha\text{-MS0}} = \frac{L_{\alpha\text{-MS}}(\max) + L_{\alpha\text{-MS}}(\min)}{2} \tag{6}$$

$$L_{S0} = \frac{L_S(\max) + L_S(\min)}{2} \tag{7}$$

$$\Delta L_{\alpha\text{-MS0}} = \frac{L_{\alpha\text{-MS}}(\max) - L_{\alpha\text{-MS}}(\min)}{2} \tag{8}$$

$$\Delta L_{S0} = \frac{L_S(\max) - L_S(\min)}{2} \tag{9}$$

Where $-1 \leqslant x_1 \leqslant 1$; $-1 \leqslant x_2 \leqslant 1$. $L_{\alpha\text{-MS}}(\max)$ and $L_{\alpha\text{-MS}}(\min)$ are the length of the longest segment and shortest segment of α-MS. $L_S(\max)$ and $L_S(\max)$ are the length of the longest segment and shortest segment of styrene. The binary quadratic regression Equation (10) was fitted using stepwise regression analysis, $R_2 = 0.982$.

$$t = 8.496 - 1.546x_1 + 1.988x_2 + 1.126x_1^2 + 3.243x_1x_2 \tag{10}$$

Fig. 9 depicts a 3D plot illustrating the regression equation, wherein the experimental points are represented by blue spheres. The results show that all six sets of data fall on the surface, indicating a good regression. The x_1 squared term coefficient

in the regression equation was 1.126, while the x_2 squared term coefficient was negligible. Additionally, the coefficient for the interaction term between the two was larger, equaling to 3.243. Evidently, the α-MS monomer unit had a nonlinear impact on the hydrogenation of the S segment, while the styrene monomer unit exhibited a positive correlation. Furthermore, the longer the chain length, the slower the hydrogenation time.

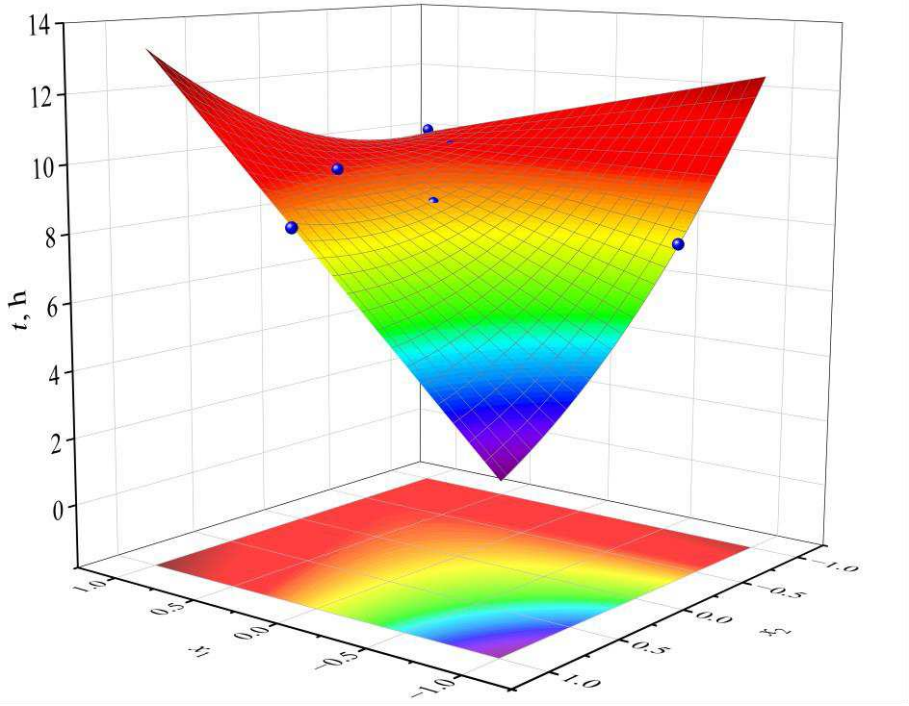

Fig. 9 3D regression projection plot (Blue spheres are experimental data)

Through simulation calculations, we use the qualitative method of Interaction Region Indicator (IRI) and the quantitative method of the electron density difference[45,46] to describe the adsorption behavior of α-SBS on the catalyst surface. In the simulation process, four representative monomer unit structures in α-SBS segment are selected: α-methylstyrene (m_1), styrene (m_2), 2,3-butadiene (m_3), and 3,4-butadiene (m_4), as shown in Fig. 10. It is assumed that each of these monomer units is adsorbed on the catalyst surface in the form of hydrogen-terminated atoms. The IRI calculation formula is given as Equation (11).[47]

$$\mathrm{IRI}(r)=\frac{|\nabla\rho(r)|}{\left[\rho(r)\right]^{a}} \tag{11}$$

Where ∇ is the gradient operator. ρ is electron density. r is the vector of z coordinates, and the empirical parameter a is chosen as 1.1. The IRI top view of the interaction between Ni and Pd metals in the catalyst is shown in Fig. 11(b), with two significant phenomena can be identified between Ni and Pd: the red region indicates the repulsive effect between metal atoms due to steric hindrance, while the blue region reveals the

strong attractive interaction of the Ni_2Pd alloy ionic bond. Fig. 11(a) presents the IRI side view and top view of the adsorption of monomer units m_1, m_2, m_3, and m_4 on the catalyst surface. From Fig. 11(a), it is evident that within the region defined by the yellow dashed lines, there are chemical bonding and van der Waals forces between the monomer units and the catalyst surface. For example, the deep blue isosurfaces within the 1 and 2 yellow circles indicate the chemical bonding between the benzene ring and the metal surface, while the 3 and 4 circles correspond to the chemical bonding between the double bond and the metal surface. Additionally, the green region represents the van der Waals interaction between saturated bonds and the metal surface.

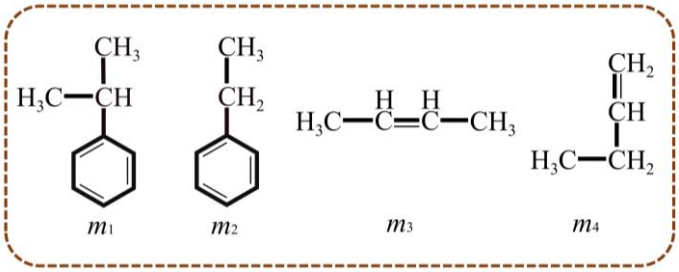

Fig. 10 Four monomeric unit structures m_1, m_2, m_3, and m_4 in α-SBS segments

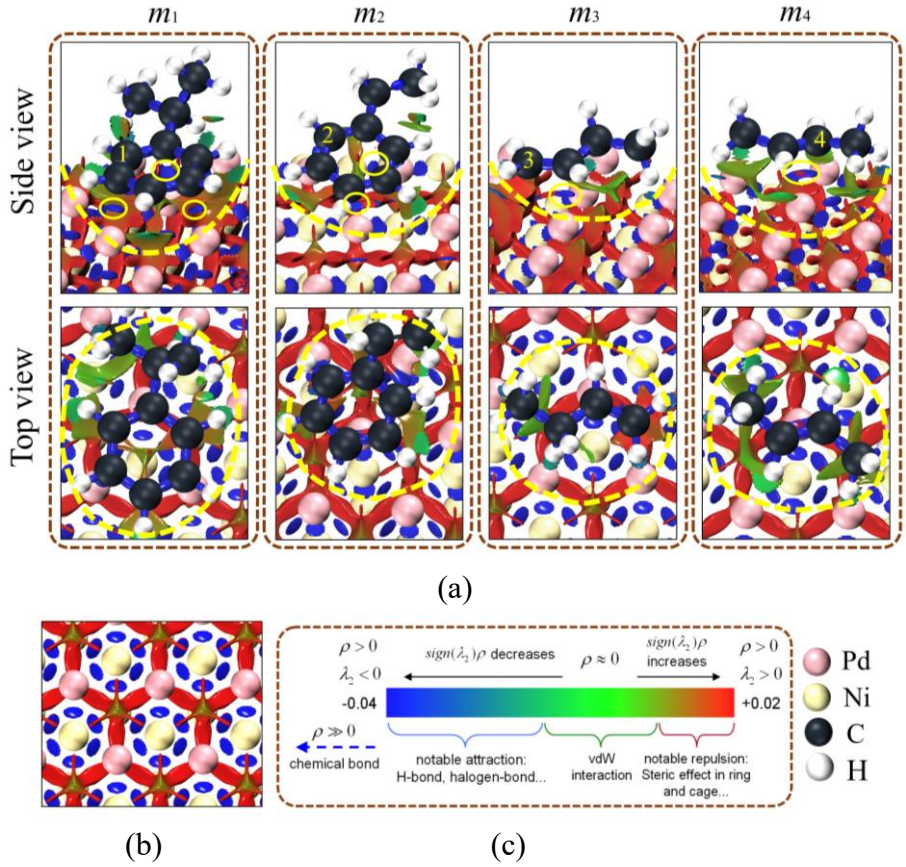

Fig. 11 (a) IRI side and top views of metal surfaces and m_1, m_2, m_3, and m_4 monomer units; (b) IRI Top view of catalyst; (c) Commonly used color scale in IRI map and common interpretation of various color ranges

To further describe the electronic shift between the metal surface of the catalyst

and four monomer unit structures, we employ the method of calculating the electron density difference[45] to quantitatively analyze the charge distribution at the interface of metal and monomer unit structures. The formula is shown in Equation (12).[47]

$$\Delta\rho_{\text{diff}}(x, y, z) = \Delta\rho_{\text{system}}(x, y, z) - \Delta\rho_{\text{surface}}(x, y, z) - \Delta\rho_{\text{adsorbate}}(x, y, z) \quad (12)$$

Where $\Delta\rho_{\text{diff}}(x,y,z)$ represents the electron density difference in Cartesian space. $\Delta\rho_{\text{system}}(x,y,z)$ represents the electron density in space when the reactant is adsorbed on the catalyst surface. $\Delta\rho_{\text{surface}}(x,y,z)$ represents the electron density in space when only the catalyst surface is present, and $\Delta\rho_{\text{adsorbate}}(x,y,z)$ represents the electron density in space when only the reactant is present.

According to the results shown in Fig. 12(a_1), electron transfer occurs when the m_1 monomer unit contacts the Ni_2Pd catalyst (Fig. S2). The local integral curve of electron density difference quantitatively describes the increase or decrease in electron density along the z coordinate direction, as shown in Fig. 12(a_2). It can be observed that the electron density difference of Pd atoms in the Ni_2Pd catalyst is positive, while the electron density difference of C atoms in the m_1 monomer unit is negative, indicating that electrons flow from C atoms to Pd atoms. The charge displacement curve in Fig. 12(a_3) further confirms this: at $z < 5.58$ Å, the net increase in electron number is 0.206; at $z > 5.58$ Å, the net decrease in electron number is 0.206. When the m_2, m_3, and m_4 monomer units contact the Ni_2Pd catalyst, electron transfer also occurs, as shown in Fig. 12(b_1), (c_1), and (d_1). From Fig. 12(b_2), (c_2), and (d_2), it can be seen that electrons flow from the C atoms in the m_2, m_3, and m_4 monomer units to the Pd atoms. The specific charge transfer situations are as follows: in Fig. 12(b_3), at $z < 5.67$ Å, the net increase in electron number is 0.195; at $z > 5.67$ Å, the net decrease in electron number is 0.195. In Fig. 12(c_3), at $z < 5.67$ Å, the net increase in electron number is 0.154; at $z > 5.67$ Å, the net decrease in electron number is 0.154. In Fig. 12(d_3), at $z < 5.57$ Å, the net increase in electron number is 0.132; at $z > 5.57$ Å, the net decrease in electron number is 0.132. When the benzene ring in the m_1 and m_2 monomer units and the C=C double bond in the m_3 and m_4 monomer units contact the surface of the Ni_2Pd catalyst, electron shifts occur, and the number of electrons obtained by the catalyst is 0.206, 0.195, 0.154, and 0.132, respectively. The charge transfer at the benzene ring is greater than that at the C=C double bond, and the α-methylstyrene monomer unit has a higher charge transfer than the styrene monomer unit, while the 2,3-butadiene monomer unit has a higher charge transfer than the 3,4-butadiene monomer unit.

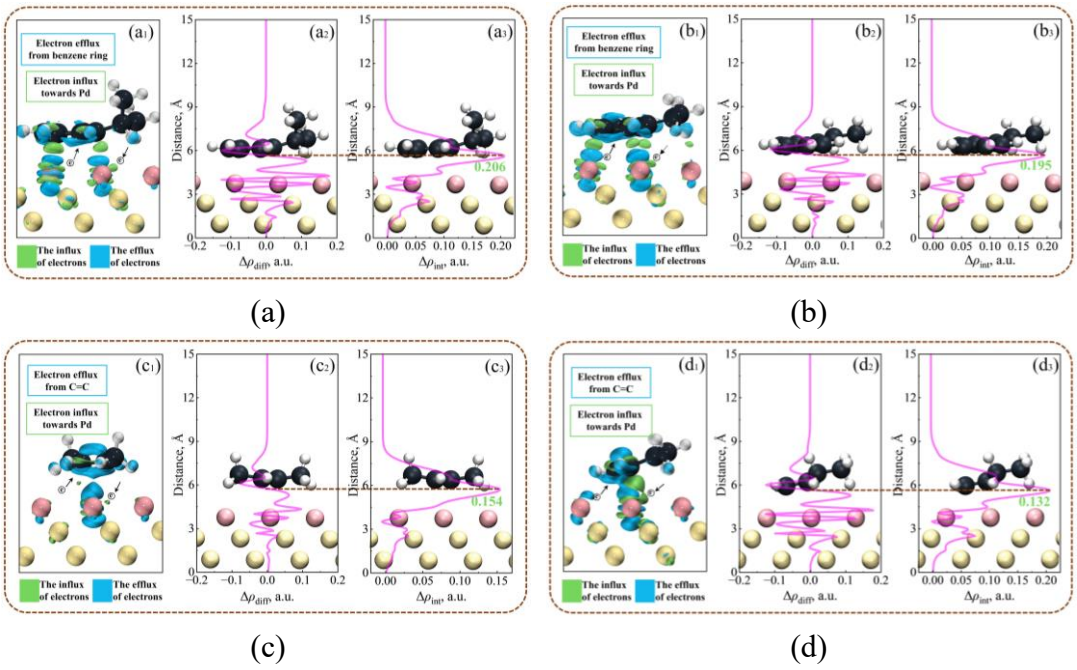

Fig. 12 (a) (b) (c) (d) Differential electron density plots and charge displacement profiles for four structures m_1, m_2, m_3, and m_4, respectively

The adsorption, activation, and desorption steps of the four monomer units, m_1, m_2, m_3, and m_4, in α-SBS on the catalyst surface will affect the ease of their hydrogenation. The interaction energy between the benzene ring[40] and double bond[48] with the catalyst surface decreases after hydrogenation saturation, allowing them to quickly desorb from the metal surface, hence ignoring the influence of desorption. Since adsorption and activation occur simultaneously on the catalyst surface, to explain the ease of activation of the four monomer units on the catalyst surface, the adsorption-activation energy E_a of the four monomer units on the catalyst surface is quantitatively calculated through DFT, as shown in Equation (13).

$$E_a = E_{adsorbate/metal} - E_{metal} - E_{adsorbate} \quad (13)$$

Where $E_{adsorbate}$ (kJ/mol) and E_{metal} (kJ/mol) represent the energy of the four monomer units before adsorption and the energy of Ni_2Pd metal, respectively. $E_{adsorbate/metal}$ (kJ/mol) represents the energy of the monomer unit-metal structure after adsorption.

The adsorption-activation energies of the four monomer units on the Ni_2Pd catalyst are calculated to be −197.2 kJ/mol, −195.1 kJ/mol, −133.2 kJ/mol, and −110.4 kJ/mol, respectively. Compared to the m_3 and m_4 monomer units with C=C double bond structures, the m_1 and m_2 monomer units with benzene ring structures exhibit stronger adsorption-activation capabilities on the catalyst. A higher adsorption activation energy indicates that the monomer unit is more difficult to activate on the catalyst surface.[49,50] Therefore, the activation ability of the m_1 and m_2 monomer units is weaker than that of the m_3 and m_4 monomer units, with the activation of α-

methylstyrene being relatively more difficult compared to styrene and the activation of 2,3-butadiene being relatively more difficult compared to 3,4-butadiene. Chen et al.[49] used DFT simulation to calculate the adsorption energies of benzene molecules on Co-M (M: Pd, Pt, and Ru) bimetallic catalysts, showing that the lower the adsorption energy of benzene molecules on the catalyst surface, the higher the hydrogenation activity of the metal catalyst towards benzene. In addition, due to the presence of the α-methyl group in the α-methylstyrene monomer unit, its adsorption activation energy is 2.1 kJ/mol higher than that of styrene, indicating that the presence of this group hinders the activation of the benzene ring. Therefore, an increase in the α-MS content in α-SBS will lead to an increase in the difficulty of activating this segment, ultimately prolonging the hydrogenation time. This result is consistent with the regression result of the equation.

3.3 Structure and Thermal Properties Analysis of Polymers

The structural changes of α-SBS1 and α-CBC1 are analyzed using FTIR, ^{1}H NMR, and ^{13}C NMR techniques. As shown in Fig. 13, α-SBS1 exhibits absorption peaks at 755 cm^{-1}, 908 cm^{-1}, and 965 cm^{-1}, which correspond to vibrations of 1,4-cis C=C, 1,2-C=C, and 1,4-trans C=C, respectively. Additionally, the peaks at 1492 cm^{-1} and 1600 cm^{-1} represent characteristic peaks of the benzene ring, while the peaks at 696 cm^{-1} and 752 cm^{-1} correspond to out-of-plane bending vibrations of C−H on the benzene ring. The in-plane bending vibrational peak is observed at 3024 cm^{-1}.[51] All of these characteristic peaks are absent in α-CBC1. Instead, the α-CBC1 spectra show characteristic signals associated with $-CH_2$ (722 cm^{-1}) after saturation of the double bond. Meanwhile, more pronounced C−H stretching vibrational peaks of cycloalkanes and alkanes appeared at 2917 cm^{-1} and 2845 cm^{-1}, thus confirming the saturation of both the benzene ring and double bond structures.

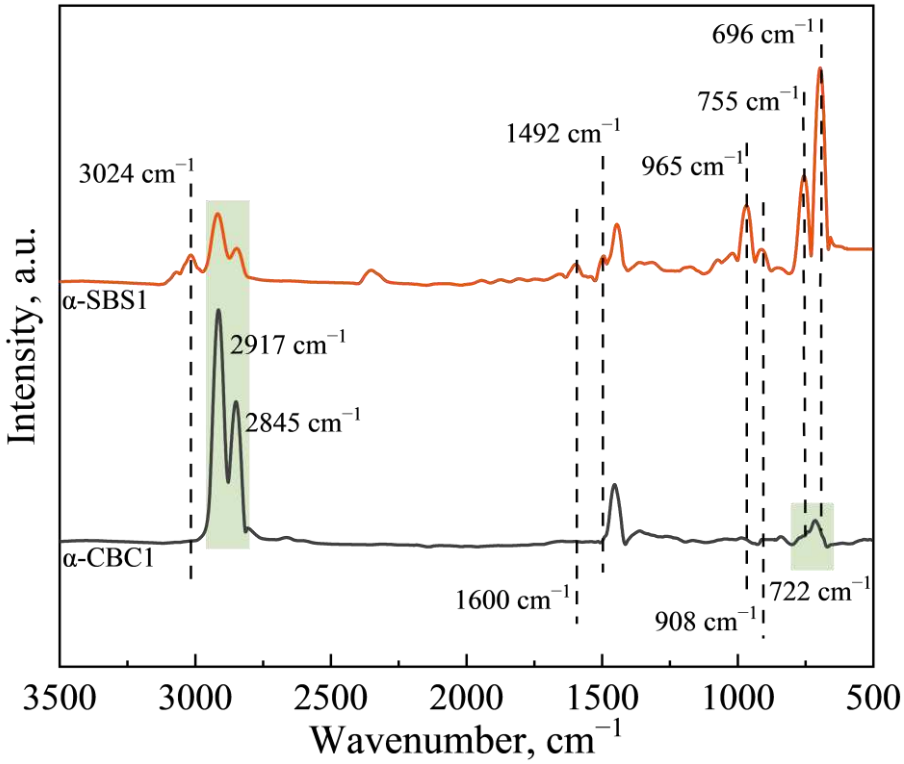

Fig. 13 Infrared absorption peak spectra of α-SBS1 and α-CBC1 samples

To further elucidate the structure of α-SBS1 and α-CBC1, we conducted ^{1}H NMR and ^{13}C NMR spectroscopic analyses. In the ^{1}H NMR spectrum (Fig. 14), the peak detected at 7.26 ppm was $CDCl_3$ solvent. Before hydrogenation, the 1,2-vinyl peaks at 4.9 ppm - 5.1 ppm, the 1,4-trans and 1,4-cis peaks at 5.37 ppm and 5.42 ppm in the α-SBS1 segment associated with the B segment, and the $-CH_2-$ peak in $-CH_2-CH=CH-CH_2-$ at 2.0 ppm all disappeared after hydrogenation. Additionally, the benzene ring peaks (6.3 ppm - 7.2 ppm)[52] associated with the S segment were completely absent upon hydrogenation. Methyl and methylene protons in all monomer units resonated in the range of 0.9 ppm - 2.4 ppm, with the overlapping peak at 1.2 ppm being the characteristic signal of α-MS.[53] In the ^{13}C NMR spectrum in (Fig. 15), the C=C peaks (130.3 ppm, 129.8 ppm, 32.8 ppm, and 27.5 ppm) of α-SBS1 disappeared, while new peaks corresponding to the $-CH_2$ (36.4 ppm, 34.7 ppm, and 30.1 ppm)[6] appeared in α-CBC1. Moreover, the peaks of the S segment (128.4 ppm and 126.1 ppm) disappeared and simultaneously transformed into cyclohexane signal peaks at 43.2 ppm and 26.4 ppm. These results were consistent with the findings of FTIR and ^{1}H NMR, indicating that the sample had reached full saturation.

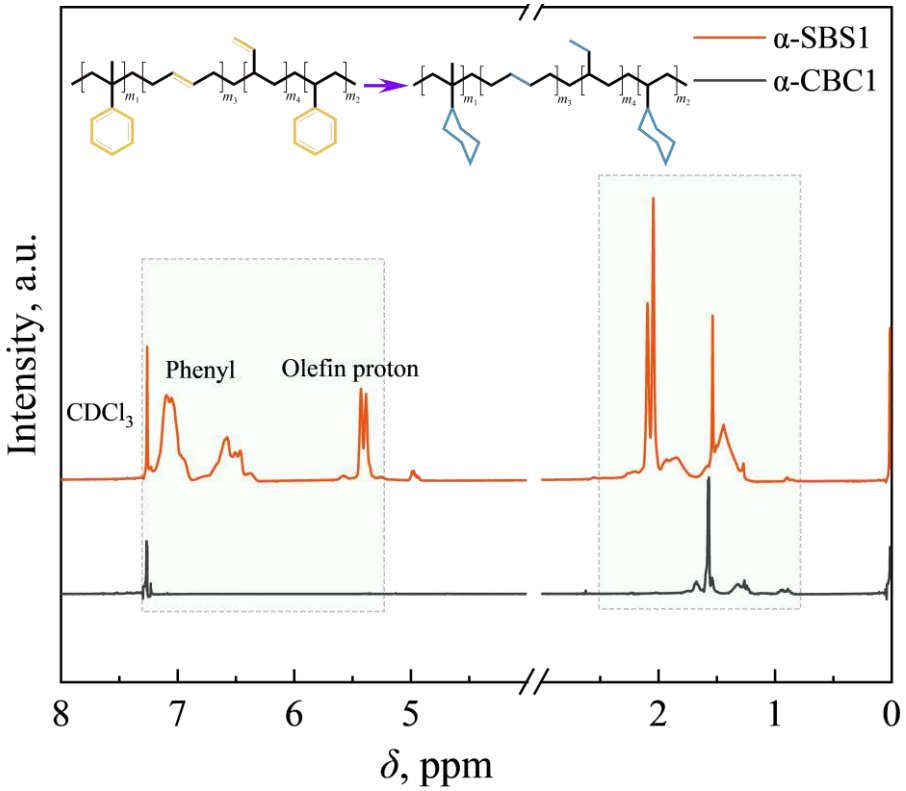

Fig. 14 ^{1}H NMR spectra of α-SBS1 before and after hydrogenation in 600 M magnetic field

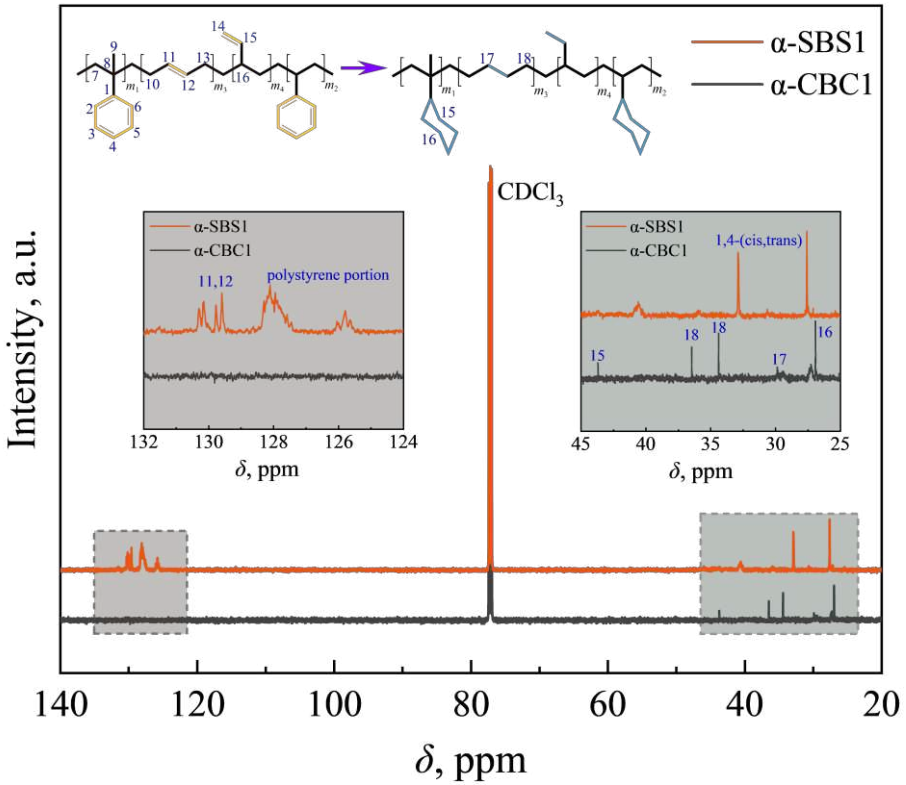

Fig. 15 ^{13}C NMR spectra of α-SBS1 before and after hydrogenation in 600 M magnetic field

The absorption of heat and exothermic processes during phase transitions are crucial factors in evaluating the thermal properties of various polymeric materials. The thermal properties of the samples before and after hydrogenation of α-SBS were

analyzed using DSC, as shown in Fig. S3. The values for T_g, T_c, and T_m were determined, and the ΔH_c and ΔH_m were calculated. These results are listed in Table 3.

Table 3 Thermal performance data for all polymers and fully hydrogenated products

No.	Polymer	T_{gB}, °C	T_{gS}, °C	T_c, °C	ΔH_c, J/g	T_m, °C	ΔH_m, J/g	χ_c, %
1	PS	/	100.0	/	/	/	/	/
1H	PCHE	/	142.0	/	/	/	/	/
2	PB	−99.4	/	−45.9	−50.9	−9.8	30.4	10.2
2H	HPB	−97.5	/	69.0	−116.8	91.1	79.0	26.9
3	SBS	−84.1	100.0	/	/	/	/	/
3H	CBC	−81.9	144.2	52.2	−8.6	88.1	13.7	4.8
4	α-SBS1	−85.6	100.3	/	/	/	/	/
4H	α-CBC1	−83.4	145.5	62.0	−18.6	98.8	14.7	5.0
5	α-SBS2	−86.4	101.1	/	/	/	/	/
5H	α-CBC2	−84.8	146.6	50.6	−4	81.3	16.2	5.5
6	α-SBS3	−85.0	101.2	/	/	/	/	/
6H	α-CBC3	−83.7	147.8	75.1	−15.3	101	23.4	8.0
7	α-SBS4	−83.8	101.6	/	/	/	/	/
7H	α-CBC4	−80.8	148.6	44.7	−7.9	81.2	13.1	4.5
8	α-SBS5	−83.3	102.0	/	/	/	/	/
8H	α-CBC5	−79.1	149.2	48.9	−6.6	89.3	14.4	4.9
9	α-SBS6	−81.1	102.5	/	/	/	/	/
9H	α-CBC6	−78.8	150.3	43.5	−10.2	81.1	10.4	3.6

The coded number in the table is the sample number before hydrogenation; The coded number followed by H indicates the sample number after hydrogenation.

The thermal properties of PS and PCHE are presented in Table 3(No.1 and No.1H). Both of which exhibit amorphous structures and only show a T_g. The T_g of PS increases from 100 °C to 142 °C after the benzene ring in the S segment is fully hydrogenated to a cyclohexyl group. Hucul et al.[54] reported that the T_g of PS increased from 105 °C to 147 °C after hydrogenation, resulting in a 42 °C increase in both cases. Partial hydrogenation of PB (No.2) resulted in the formation of HPB (No.2H, *HD*=80 %), which leads to an increase in χ_c from 10.2 % to 26.9 % due to the transformation of 80 % of the B segment to PE. In the case of SBS (No.3), the T_g of the B segment (−84.1 °C) is 15.3 °C higher than that of PB (−99.4 °C). This difference can be attributed not only to the shorter length of the B segment in SBS compared to PB but also to the variation in the content of 1,4-cis, 1,4-trans, and 1,2-segments between the two materials. These differences prevent the B segment in SBS from exhibiting crystallization behavior. Similarly, none of the B segments in α-SBS1 - 6 shows crystallization behavior. As a result, the T_g of CBC increased to −81.9 °C. Additionally, the PE segment displays crystallization behavior, with a degree of crystallinity of 4.8 % and a crystallization temperature of 52.2 °C. Due to the presence of the PE segment, the T_g of the S segment

increases from 100 °C to 144.2 °C after hydrogenation, which is 2.2 °C higher than that of PCHE. As shown in Table 3, the B segment in α-SBS1 (No.4) exhibits a T_g of −85.6 °C, which is slightly increased after full hydrogenation. It also shows crystallization behavior, with a degree of crystallinity of 5.0 % and a crystallization temperature of 62.0 °C. Comparison with PS in Table 3 shows that the T_g of the S segment (100.3 °C) is 0.3 °C higher than that of PS due to the presence of α-methyl[55] in α-MS. The α-methyl not only occupies a spatial position but also affects the segment motion, leading to an increased T_g of the S segment. After the reaction, the T_g of this segment increases to 145.5 °C, which is 3.5 °C higher than that of PCHE. This increase can be attributed to the significant presence of the cyclohexane group and the synergistic effect of α-methyl.

Moreover, Fig. 16(a) plots the T_g versus α-MS content before and after hydrogenation of the S segment, comparing No.4 to No.9 in Table 3. The T_g of the S segment in α-SBS and α-CBC shows a nearly linear increasing relationship with increasing α-MS content, with increasing ratios of 0.63 °C/(mol%) and 1.49 °C/(mol%), respectively. This clearly demonstrates that the introduction of α-MS not only increases the T_g of the S segment in α-SBS but also has an even greater impact on the T_g of α-CBC after hydrogenation. This conclusion is strongly supported in Fig. 16(b). It can be anticipated that augmenting the α-MS content and fully hydrogenating α-CBC will result in a significant elevation of the glass transition temperature of α-CBC.

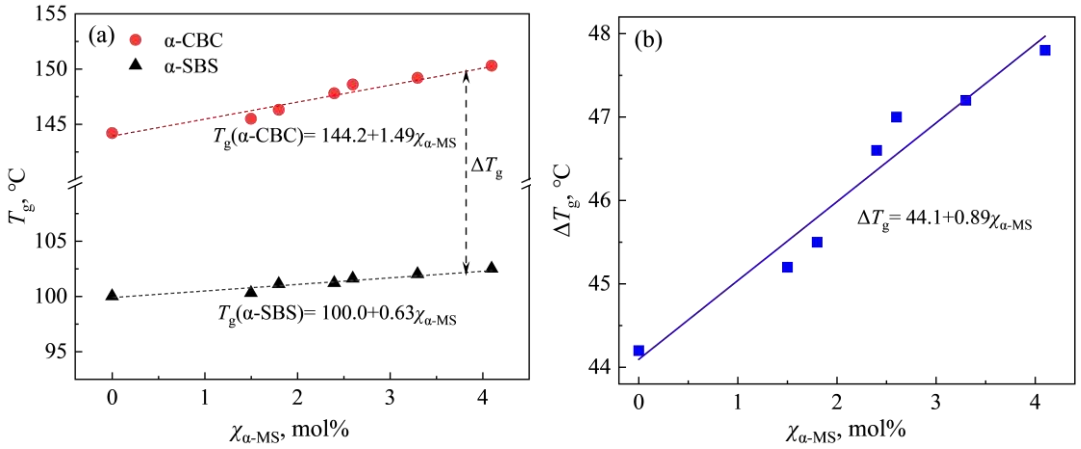

Fig. 16 (a) Dependence of the T_g of the S segment with the $\chi_{α\text{-MS}}$ in α-SBS and α-CBC; (b) Variation of the ΔT_g with the $\chi_{α\text{-MS}}$ (where ΔT_g is the difference in the S segment T_g before and after full hydrogenation of α-SBS)

4. CONCLUSION

Ni and Pd bimetallic catalysts supported on N-doped carbon nanotubes (NCNTs) were obtained using an equal volume impregnation method, resulting in Ni_xPd/NCNT@MFN. SEM results showed that after the growth of NCNTs, the morphology of MFN changed from smooth to rough, and EDS analysis indicated that N and C elements were presented with an N/C mass ratio of 2.17 % in NCNTs. TEM results revealed that Ni and Pd existed in the form of an alloy with a crystal plane spacing of 0.216 nm, and the average particle size was 3.91 nm. Under the catalysis of Ni_2Pd/NCNT@MFN, α-SBS could be completely hydrogenated to α-CBC. The hydrogenation activity of C=C double bonds in α-SBS was significantly higher than that of benzene rings. The hydrogenation of butadiene segments in α-SBS resulted in the formation of a regular arrangement of crystalline polyethylene segments, reducing the solubility of the polymer. Therefore, the C=C to be hydrogenated spent a minimal amount of time on the catalyst surface, affecting the hydrogenation rate. The longer the butadiene segments in α-SBS, the longer the hydrogenation time. Additionally, the length of the α-methylstyrene and styrene segments also had a similar relationship with the hydrogenation time. The results of the quadratic regression equation indicated a negative effect of the α-methyl group on the hydrogenation of the phenyl ring. DFT calculations revealed the interaction between the four monomer units in α-SBS and the catalyst, and the adsorption-activation energy of α-methylstyrene was the highest, indicating that the presence of the α-methyl group hindered the activation of the benzene ring. Moreover, as the content of the α-methylstyrene segment increased, the hydrogenation time became longer.

After hydrogenation, the benzene ring, 1,4-butadiene, and 1,2-butadiene in α-SBS were all saturated, resulting in the crystalline behavior of α-CBC due to the presence of polyethylene segments, along with the corresponding crystallization temperature and degree. Meanwhile, the introduction of α-methyl in the styrene segment further increased the glass transition temperature of α-CBC. The conclusions obtained in this study have significant theoretical guidance for the synthesis of novel α-CBC.

5. REFERENCES

[1] Cabral H, Miyata K, Osada K, Kataoka K (2018) Block Copolymer Micelles in N anomedicine Applications. Chemical Reviews 118: 6844-6892.
http://dx.doi.org/10.1021/acs.chemrev.8b00199

[2] Yang J-X, Pan L, Ma Z, Wang B, Li Y-S (2019) Syntheses and properties of ABA, CBA, and CBC triblock copolymers based thermoplastic elastomers with glassy (A), elastomeric (B), and crystalline (C) blocks. Journal of Macromolecular Science, Part A 56: 225-233.
http://dx.doi.org/10.1080/10601325.2019.1565544

[3] Yan J-Y, Cao G-P (2023) Advances in the Catalytic Hydrogenation and Properties of Unsaturated Polymers. Macromolecules 56: 3774-3808.
http://dx.doi.org/10.1021/acs.macromol.2c02333

[4] Schneider Y, Lynd N A, Kramer E J, Bazan G C (2009) Novel Elastomers Prepare d by Grafting n-Butyl Acrylate from Polyethylene Macroinitiator Copolymers. Macro molecules 42: 8763-8768.
http://dx.doi.org/10.1021/ma901796f

[5] Ban H T, Kase T, Kawabe M, Miyazawa A, Ishihara T, Hagihara H, Tsunogae Y, Murata M, Shiono T (2006) A New Approach to Styrenic Thermoplastic Elastomers: S ynthesis and Characterization of Crystalline Styrene-Butadiene-Styrene Triblock Copo lymers. Macromolecules 39: 171-176.
http://dx.doi.org/10.1021/ma051576h

[6] HAHN S F (1992) An Improved Method for the Diimide Hydrogenation of Butad iene and Isoprene Containing Polymers. Journal of Polymer Science Part A Polymer C hemistry 30: 397-408.
http://dx.doi.org/10.1002/pola.1992.080300307

[7] Harwood H J, Russell D B, Verthe J J A, Zymona J (1973) Diimide as a Reagent f or the Hydrogenation of Unsaturated Polymers. Die Makromolekulare Chemie 163: 1-12.
http://dx.doi.org/10.1002/macp.1973.021630101

[8] Menossi M, Ciolino A, Quinzani L M, Zabaloy M S, Milanesio J M (2022) Hydro genation of Polybutadiene at High Pressure. Industrial & Engineering Chemistry Rese arch 61: 236-248.
http://dx.doi.org/10.1021/acs.iecr.1c03873

[9] Mango L A, Lenz R W (1973) Hydrogenation of Unsaturated Polymers with Diim ide. Die Makromolekulare Chemie 163: 13-36.
http://dx.doi.org/10.1002/macp.1973.021630102

[10] Mohammadi N A, Rempel G L (1989) Homogeneous Catalytic Hydrogenation of Polybutadiene. Journal of Mofeculor Catalysis 50: 259-275.
http://dx.doi.org/10.1016/0304-5102(89)80284-6

[11] SABATA S, HETFLEJS J (2002) Hydrogenation of Low Molar Mass OH-Teleche lic Polybutadienes Catalyzed by Homogeneous Ziegler Nickel Catalysts. Journal of A pplied Polymer Science 85: 1185-1193.
http://dx.doi.org/10.1002/app.10712

[12] Poshyachinda S, Kanitthanon V (1994) FT Raman spectroscopic study of the diim ide hydrogenation of cis-polybutadiene: some evidence of cis-truns isomerization. Spe ctrochimica Acta Part A: Molecular Spectroscopy 50: 2011-2017.
http://dx.doi.org/10.1016/0584-8539(94)80213-0

[13] Chang J-R, Huang S-M (1998) Pd/Al_2O_3 Catalysts for Selective Hydrogenation of

Polystyrene-block-polybutadiene-block-polystyrene Thermoplastic Elastomers. Industrial & Engineering Chemistry Research 37: 1220-1227.
http://dx.doi.org/10.1021/ie9705665
[14] KRIGAS T M, CARELLA J M, STRUGLINSKI M J, CRIST B, GRAESSLEY W W (1985) Model Copolymers of Ethylene with Butene-1 Made by Hydrogenation of Polybutadiene: Chemical Composition and Selected Physical Properties. Polymer Physics Edition 23: 509-520.
http://dx.doi.org/10.1002/pol.1985.180230308
[15] Wang M, Wang Y, Mou X, Lin R, Ding Y (2022) Design strategies and structure-performance relationships of heterogeneous catalysts for selective hydrogenation of 1,3-butadiene. Chinese Journal of Catalysis 43: 1017-1041.
http://dx.doi.org/10.1016/S1872-2067
[16] Wei S, Cheong W-C, Peng Q, Gu L, Li A, Liu J-C, Li Z, Chen W, Gong Y, Wang Y, Zheng L, Xiao H, Li J, Chen C, Han X, Li Y (2018) Direct observation of noble metal nanoparticles transforming to thermally stable single atoms. Nature Nanotechnology 13: 856-861.
http://dx.doi.org/10.1038/s41565-018-0197-9
[17] Zhao Y-J, Zhou J, Zhang J-G, Li D-Y, Wang S-D (2008) Selective Hydrogenation of Benzene to Cyclohexene on a Ru/Al_2O_3/Cordierite Monolithic Catalyst: Effect of Mass Transfer on the Catalytic Performance. Industrial & Engineering Chemistry Research 47: 4641-4647.
http://dx.doi.org/10.1021/ie071574g
[18] Boger T, Heibel A K, Sorensen C M (2004) Monolithic Catalysts for the Chemical Industry. Industrial & Engineering Chemistry Research 43: 4602-4611.
http://dx.doi.org/10.1021/ie030730q
[19] Luo Z-H, Feng M, Lu H, Kong X-X, Cao G-P (2019) Nitrile Butadiene Rubber Hydrogenation over A Monolithic Pd/CNTs@Nickel Foam Catalysts: Tunable CNTs Morphology Effect on Catalytic Performance. Industrial & Engineering Chemistry Research 58: 1812-1822.
http://dx.doi.org/10.1021/acs.iecr.8b04688
[20] Feng M, Luo Z-H, Yi S, Lu H, Lu C, Li C-Y, Zhao J-L, Cao G-P (2018) Palladium Supported on Carbon Nanotubes Decorated Nickel Foam as the Catalytic Stirrer in Heterogeneous Hydrogenation of Polystyrene. Industrial & Engineering Chemistry Research 57: 16227-16238.
http://dx.doi.org/10.1021/acs.iecr.8b03810
[21] Shen J, Hayes R E, Wu X, Semagina N (2015) 100° Temperature Reduction of Wet Methane Combustion: Highly Active Pd-Ni/Al_2O_3 Catalyst versus Pd/$NiAl_2O_4$. ACS Catalysis 5: 2916-2920.
http://dx.doi.org/10.1021/acscatal.5b00060
[22] Rai R K, Gupta K, Tyagi D, Mahata A, Behrens S, Yang X, Xu Q, Pathakad B, Singh S K (2016) Access to highly active Ni-Pd bimetallic nanoparticle catalysts for C–C coupling reactions. Catalysis Science & Technology 6: 5567-5579.
http://dx.doi.org/10.1039/C6CY00037A
[23] Jiang Y, Li Q, Li X, Wang X, Dong S, Li J, Hou L, Jiao T, Wang Y, Gao F (2021) Three-Dimensional Network Pd-Ni/γ-Al_2O_3 Catalysts for Highly Active Catalytic Hydrogenation of Nitrobenzene to Aniline under Mild Conditions. ACS Omega 6: 9780-9790.
http://dx.doi.org/10.1021/acsomega.1c00441
[24] Ho P H, Woo J-W, Ilmasani R F, Han J, Olsson L (2021) The role of Pd-Pt Interactions in the Oxidation and Sulfur Resistance of Bimetallic Pd-Pt/γ-Al_2O_3 Diesel Oxida

tion Catalysts. Industrial & Engineering Chemistry Research 60: 6596-6612.
http://dx.doi.org/10.1021/acs.iecr.0c05622
[25] Sharma A K, Mehara P, Das P (2022) Recent Advances in Supported Bimetallic Pd-Au Catalysts: Development and Applications in Organic Synthesis with Focused Catalytic Action Study. ACS Catalysis 12: 6672-6701.
http://dx.doi.org/10.1021/acscatal.2c00725
[26] Chen L Y, Chen N, Hou Y, Wang Z C, Lv S H, Fujita T, Jiang J H, Hirata A, Chen M W (2013) Geometrically Controlled Nanoporous PdAu Bimetallic Catalysts with Tunable Pd/Au Ratio for Direct Ethanol Fuel Cells. ACS Catalysis 3: 1220-1230.
http://dx.doi.org/10.1021/cs400135k
[27] Zhang Z, Lu Z-H, Chen X (2015) Ultrafine Ni-Pt Alloy Nanoparticles Grown on Graphene as Highly Efficient Catalyst for Complete Hydrogen Generation from Hydrazine Borane. ACS Sustainable Chemistry & Engineering 3: 1255-1261.
http://dx.doi.org/10.1021/acssuschemeng.5b00250
[28] Song S-F, Guo Y-T, Wang R-Y, Fu Z-S, Xu J-T, Fan Z-Q (2016) Synthesis and Crystallization Behavior of Equisequential ADMET Polyethylene Containing Arylene Ether Defects: Remarkable Effects of Substitution Position and Arylene Size. Macromolecules 49: 6001-6011.
http://dx.doi.org/10.1021/acs.macromol.6b01324
[29] Santin C K, Jacobi M M, Schuster R H, Santoso M (2010) Thermal behavior of partially hydrogenated polydienes by p-toluenesulfonylhydrazide. J Therm Anal Calorim 101: 273-279.
http://dx.doi.org/10.1007/s10973-010-0750-8
[30] Perdew J P, Burke K, Ernzerhof M (1996) Generalized Gradient Approximation Made Simple. Physical review letters 77: 3865-3868.
http://dx.doi.org/10.1103/PhysRevLett.77.3865
[31] Hutter J, Iannuzzi M, Schiffmann F, VandeVondele J (2014) CP2K: atomistic simulations of condensed matter systems. WIREs Computational Molecular Science 4: 15-25.
http://dx.doi.org/10.1002/wcms.1159
[32] Lu T, Chen F (2012) Multiwfn: A Multifunctional Wavefunction Analyzer. Journal of Computational Chemistry 33: 580-592.
http://dx.doi.org/10.1002/jcc.22885
[33] He Z, Dong B, Wang W, Yang G, Cao Y, Wang H, Yang Y, Wang Q, Peng F, Yu H (2019) Elucidating Interaction between Palladium and N-Doped Carbon Nanotubes: Effect of Electronic Property on Activity for Nitrobenzene Hydrogenation. ACS Catalysis 9: 2893-2901.
http://dx.doi.org/10.1021/acscatal.8b03965
[34] Huynh T-T, Huang W-H, Tsai M-C, Nugraha M, Haw S-C, Lee J-F, Su W-N, Hwang B J (2021) Synergistic Hybrid Support Comprising TiO_2-Carbon and Ordered PdNi Alloy for Direct Hydrogen Peroxide Synthesis. ACS Catalysis 11: 8407-8416.
http://dx.doi.org/10.1021/acscatal.0c05485
[35] Chen L, Guo H, Fujita T, Hirata A, Zhang W, Inoue A, Chen M (2011) Nanoporous PdNi Bimetallic Catalyst with Enhanced Electrocatalytic Performances for Electro-oxidation and Oxygen Reduction Reactions. ADVANCED FUNCTIONAL MATERIALS 21: 4364-4370.
http://dx.doi.org/10.1002/adfm.201101227
[36] Goswami C, Saikia H, Tada K, Tanaka S, Sudarsanam P, Bhargava S K, Bharali P (2020) Bimetallic Palladium-Nickel Nanoparticles Anchored on Carbon as High-Performance Electrocatalysts for Oxygen Reduction and Formic Acid Oxidation Reactions.

Acs Applied Energy Materials 3: 9285-9295.
http://dx.doi.org/10.1021/acsaem.0c01622
[37]Horiuti J, Polanyi M (1933) A Catalysed Reaction of Hydrogen with Water. Natur e 132: 819.
http://dx.doi.org/10.1038/132819a0
[38]Lonergan W W, Vlachos D G, Chen J G (2010) Correlating extent of Pt-Ni bond f ormation with low-temperature hydrogenation of benzene and 1,3-butadiene over supp orted Pt/Ni bimetallic catalysts. Journal of Catalysis 271: 239-250.
http://dx.doi.org/10.1016/j.jcat.2010.01.019
[39]Han K-Y, Cao G-P, Zuo H-R (2015) Hydrogenation of commercial polystyrene on Pd/TiO_2 monolithic ceramic foam catalysts: catalytic performance and enhanced inter nal mass transfer. Reaction Kinetics, Mechanisms and Catalysis 114: 501-517.
http://dx.doi.org/10.1007/s11144-014-0793-0
[40]Feng M, Lu H, Li C-Y, Cao G-P (2019) Carbon Nanotube Modified Ceramic Foa ms as Structured Palladium Supports for Polystyrene Hydrogenation. Industrial & Eng ineering Chemistry Research 58: 10793-10803.
http://dx.doi.org/10.1021/acs.iecr.9b01228
[41]Petzetakis N, Stone G M, Balsara N P (2014) Synthesis of Well-Defined Polyethy lene-Polydimethylsiloxane- Polyethylene Triblock Copolymers by Diimide-Based Hy drogenation of Polybutadiene Blocks. Macromolecules 47: 4151-4159.
http://dx.doi.org/10.1021/ma500686k
[42]Kong X, Silveira M D L V, Zhao L, Choi P (2002) A Pseudo Equation-of-State Ap proach for the Estimation of Solubility Parameters of Polyethylene by Inverse Gas Chr omatography. Macromolecules 35: 8586-8590.
http://dx.doi.org/10.1021/ma020508h
[43]SARKAR M D, DE P P, BHOWMICK A K (1998) Influence of Styrene Content o n the Hydrogenation of Styrene-Butadiene Copolymer. Journal of Applied Polymer Sc ience 71: 1581-1595.
http://dx.doi.org/10.1002/(sici)1097-4628(19990307)71:10<1581::aid-app6>3.0.co;2-c
[44]Fetters L J, Hadjichristidis N, Lindner J S, Mays J W (1994) Molecular Weight De pendence of Hydrodynamic and Thermodynamic Properties for Well-Defined Linear P olymers in Solution. Journal of physical and chemical reference data 23: 619-640.
http://dx.doi.org/10.1063/1.555949
[45]Yoon Y, Rousseau R, Weber R S, Mei D, Lercher J A (2014) First-Principles Stud y of Phenol Hydrogenation on Pt and Ni Catalysts in Aqueous Phase. Journal of the A merican Chemical Society 136: 10287-10298.
http://dx.doi.org/10.1021/ja501592y
[46]Chen Q, Wang X, Yi P, Zhang P, Zhang L, Wu M, Pan B (2021) Key roles of elect ron cloud density and configuration in the adsorption of sulfonamide antibiotics on car bonaceous materials: Molecular dynamics and quantum chemical investigations. Appli ed Surface Science 536: 147757-147769.
http://dx.doi.org/10.1016/j.apsusc.2020.147757
[47]Lu T, Chen Q (2021) Interaction Region Indicator: A Simple Real Space Function Clearly Revealing Both Chemical Bonds and Weak Interactions. Chemistry−Methods 1: 231-239.
http://dx.doi.org/10.1002/cmtd.202100007
[48]Nayakasinghe M T, Xu Y, Zaera F (2023) Acrolein Hydrogenation Catalyzed by P t(111): Effect of Carbonaceous Deposits on Kinetics. ACS Catalysis 13: 14080-14089.
http://dx.doi.org/10.1021/acscatal.3c03870

[49] Lu S, Menning C A, Zhu Y, Chen J G (2009) Correlating Benzene Hydrogenation Activity with Binding Energies of Hydrogen and Benzene on Co-Based Bimetallic Catalysts. ChemPhysChem 10: 1763-1765.
http://dx.doi.org/10.1002/cphc.200900139
[50] Chen J G, Menning C A, Zellner M B (2008) Monolayer bimetallic surfaces: Experimental and theoretical studies of trends in electronic and chemical properties. Surface Science Reports 63: 201-254.
http://dx.doi.org/10.1016/j.surfrep.2008.02.001
[51] Xicohtencatl-Serrano H, ıa-Leiner M G, Cabrera-Ortiz A, ajera R H-N (2014) Synthesis and Characterization of Poly(styrene-b-[(butadiene)$_{1-x}$-(ethylene-co-butylene)$_x$]-b-styrene) Star-Like Molecular Polymers Produced by Partial Hydrogenation of SBS. POLYMER ENGINEERING AND SCIENCE 47: 2332-2344.
http://dx.doi.org/10.1002/pen.23796
[52] Wei R, Luo Y, Zeng W, Wang F, Xu S (2012) Styrene-Butadiene-Styrene Triblock Copolymer Latex via Reversible Addition-Fragmentation Chain Transfer Miniemulsion Polymerization. Industrial & Engineering Chemistry Research 51: 15530-15535.
http://dx.doi.org/10.1021/ie302067n
[53] Mühl J, Srica V, Jarm V, Kovac-Filipovic M (1990) ^{1}H NMR Composition Analysis of Styrene-α-Methylstyrene-Butadiene Terpolymer. Industrial & Engineering Chemistry Research 29: 707-709.
http://dx.doi.org/10.1021/ie00100a035
[54] Hucul B D A, Hahn S F (2000) Catalytic Hydrogenation of Polystyrene. Advanced Materials 12: 1855-1859.
http://dx.doi.org/10.1002/1521-4095(200012)12:23<1855::AID-ADMA1855>3.0.CO;2-P
[55] XU J J, NGUYEN B T, BATES F S, HAHN S F (2003) Hydrogenated Poly(styrene-co-α-methylstyrene) Polymers: A New Class of High Glass-Transition-Temperature Polyolefins. Journal of Polymer Science: Part B: Polymer Physics 41: 725-735.
http://dx.doi.org/10.1002/polb.10425

Supplementary Files

This is a list of supplementary files associated with this preprint. Click to download.

- SI.docx
- declarationStatement.docx